UNIVERSITÄT
LEIPZIG

REPORT
Halbleiterphysik
Semiconductor Physics
2023

The Semiconductor Physics Group of Universität Leipzig, Report 2023
M. Grundmann (Ed.)

Technical Editor: Anja Heck

This work is subject to copyright. All rights are reserved.
© Universität Leipzig 2024

online available at
http://research.uni-leipzig.de/hlp/

Front cover
SEM image of the Au mask for the fabrication of the grating.

Back cover
Recently published.

Abteilung Halbleiterphysik

Felix-Bloch-Institut für Festkörperphysik

Fakultät für Physik und Erdsystemwissenschaften

Universität Leipzig

Semiconductor Physics Group

Felix Bloch Institute for Solid State Physics

Faculty of Physics and Earth System Sciences

Universität Leipzig

Report 2023

Address

Semiconductor Physics Group

Linnéstraße 5
D-04103 Leipzig, Germany

Phone: +49 341 97-32650
Fax: +49 341 97-32668
WWW: http://research.uni-leipzig.de/hlp/

Mailing address: Postfach 230001, D-04081 Leipzig, Germany

Preface

Welcome to the 2023 research report of the Semiconductor Physics Group. We invite you to explore our findings and innovations from the past year. Dive into our detailed results and insights, and we hope you discover something that captivates your interest and inspires further inquiry.

The Fall School 2023 was on "Quantum Computing" in the framework of the Graduate School BuildMona stream "Quantum Coherent Structures". From hardware aspects to use cases in supply chain management, a broad spectrum of topics was covered, finished off with a hands-on with the Universität Leipzig NV centers quantum computer.

A new high frequency wafer prober was installed and is now operational, suited to test our circuits and circuit boards up to 30 GHz. Using this machine we can optimize the control of NV center quantum processors and also integrated circuits based on our thin film diodes and transistors, in particular with small gate structures (possible with next year's installation of a new nano-lithography).

New results on doping have been obtained, including Zr-doped α-Ga_2O_3, Zn_2GeO_4:Mn and oxygen in CuI. Novel structures could be fabricated using our combinatorial epi-

taxy methods and In_2O_3 based MESFETs could be fabricated using oxygen plasma treatment for the suppression of surface charges. Noteworthy is also the 41 page review on "Electromagnetic Waves in Crystals: The Presence of Exceptional Points" by Chris Sturm (Adv. Photonics Res. 2300235 (2024)).

We are thrilled to present numerous exciting results achieved in collaboration with our esteemed colleagues nationally and around the globe. Our work would not have been possible without the generous support of our funding agencies, especially the Deutsche Forschungsgemeinschaft (DFG) and the Bundesministerium für Bildung und Forschung (BMBF). We extend our deepest gratitude to these organizations for their invaluable contributions and unwavering support.

Leipzig, *Marius Grundmann*
July 2024

Contents

I Report of the Semiconductor Physics Group 13

1 Structure and Staff of the Semiconductor Physics Group 15

2 Reports 17

2.1 An Analytical Approximation for the Space Charge Region Beyond the Abrupt Approximation . . . 17
2.2 Diffused oxygen as dominating shallow acceptor in p-type copper iodide thin films . . . 19
2.3 Heteroepitaxial (00.1) Mn^{2+}-Doped Zn_2GeO_4 Green-Emitting Phosphor Thin Films Grown on C-Plane Sapphire . . . 21
2.4 Exploration of Zr doping in pulsed laser deposited α-Ga_2O_3 for device applications . . . 25
2.5 Demonstration of Two Multi-component Target Ablation Approaches and Their Application in Pulsed Laser Deposition . . . 27
2.6 Oxygen Plasma Treatment to Enable Indium Oxide MESFET Devices . 29
2.7 Growth of κ-$([Al,In]_xGa_{1-x})_2O_3$ Quantum Wells and Their Potential for Quantum-Well Infrared Photodetectors . . . 30
2.8 Defect level in κ-Ga_2O_3 revealed by thermal admittance spectroscopy . 32
2.9 Cation segregation observed in an $(In,Ga)_2O_3$ material thin film library beyond the miscibility limit of the bixbyite structure . . . 33
2.10 Phonon Eigenvector reversal in CuBrI alloy . . . 35
2.11 Two-photon absorption channels in CuI . . . 36
2.12 Emission from propagating Bloch surface wave polaritons . . . 38
2.13 Optimization of vertically graded $Mg_xZn_{1-x}O$ layers for the use in wavemeters . . . 41
2.14 Exceptional points in optically anisotropic materials . . . 43

3 Funding, Organizational Duties, External Cooperations 45

3.1 Funding . . . 45
3.2 Organizational Duties . . . 46
3.3 External Cooperations . . . 47

4 Publications 51

5 Graduations 57

6 Guests 59

Author Index **61**

I

Report of the Semiconductor Physics Group

1

Structure and Staff of the Semiconductor Physics Group

Prof. Dr. Marius Grundmann

Secretary/Administration

Anja Heck
Johanna Lendewig
Birgit Wendisch

Technical staff

Dipl.-Phys. Gabriele Benndorf
Monika Hahn
Dipl.-Ing. Holger Hochmuth
Axel Märcker
M.Sc. Friedericke Pielenz
Dr. Daniel Splith
Dr. Lukas Trefflich

Academic staff

Dr. Carola Emminger
Prof. Dr. Michael Lorenz
Dr. Sijun Luo
PD Dr. Rainer Pickenhain (retired)
Prof. Dr. Bernd Rheinländer (retired)
Dr. Chris Sturm
Dr. Sophie Vogt
PD Dr. Holger von Wenckstern

PhD candidates

Michael Bar, M.Sc.
Jorrit Bredow, M.Sc.

Yang Chen, M.Sc.
Christiane Dethloff, M.Sc.
Sebastian Henn, M.Sc.
Ron Hildebrandt, M.Sc.
Tanja Jawinski, M.Sc.
Arne Jörns, M.Sc.
Evgeny Krüger, M.Sc.
Oliver Lahr, M.Sc.
Andreas Müller, M.Sc.
Clemens Petersen, M.Sc.
Fabian Schöppach, M.Sc.
Philipp Storm, M.Sc.
Tillmann Stralka, M.Sc.
Laurenz Thyen, M.Sc.
Arthur Rubin Witte, M.Sc.
Jingjing Yu, M.Sc. (guest, CSC)

Students

Mauricio Bassallo
Simon Briesenick
Martin Callmeier
Felix-Florian Delatowski
Visar Demiri
Jonas Elz
Doyeon Jin
Khanim Karimova
Bastian Klaus
Sebastian Köpp
Ana Lucia Pereira Brenes
Caspar Pirker

2

Reports

2.1 An Analytical Approximation for the Space Charge Region Beyond the Abrupt Approximation

M. Grundmann

We have revisited the problem of the potential, electrical field and charge density in a space charge region. Within the Boltzmann approximation, the asymptotic solution is found analytically. The exact solution everywhere can be found from numerically integrating an analytical function. A popular approximation is the *abrupt* approximation. We have worked out a better analytical approximation that mimics the tail of thermal carriers fairly well [1].

The one-dimensional problem of the potential ϕ in a Schottky diode for the n-doped semiconductor ($x \geq 0$) is

$$\phi''(x) = -\frac{\rho(x)}{\epsilon_s} \ . \tag{2.1}$$

Within the Boltzmann approximation, the Poisson equation (2.1) must be consistent with

$$\rho(x) = e\, N_D(x) \left(1 - \exp\left[\beta\, \phi(x)\right]\right) \ . \tag{2.2}$$

Here, $\beta = e/(kT)$ (e denotes the (positive) electron charge, k denotes the Boltzmann constant and T denotes the temperature) and N_D denotes the (homogeneous) donor concentration. The combined equations (2.1) and (2.2) are not integrable analytically.

For our novel analytical solution, we use the Ansatz ($\rho_0 = e\, N_D$),

$$\tilde{\rho}(x) = \frac{\rho_0}{1 + \exp\left[-(w' - x)/L'_D\right]} \tag{2.3}$$

for the charge density with a length $L'_D \approx L_D$ that has approximately the correct asymptotic behavior, $\rho \propto \exp(-x/L_D)$. L_D is the Debye length $L_D = \sqrt{(\epsilon_s\, k\, T)/(e^2\, N_D)}$. We note that this 'Fermi' distribution is used in nuclear physics as radial charge distribution model.

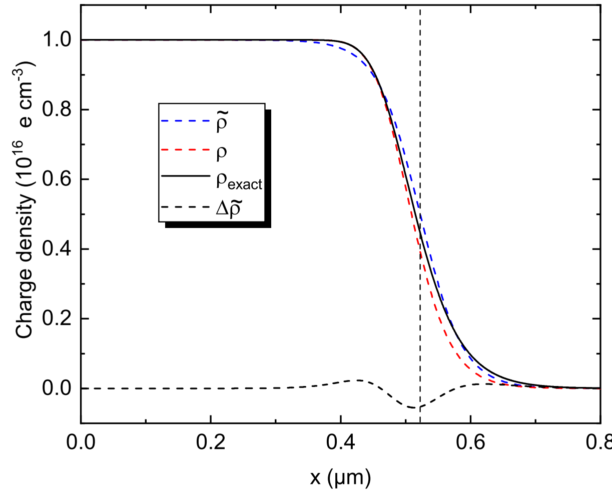

Figure 2.1: Charge distribution for the exact (numerical) solution (*solid black line*, for a Schottky diode with parameters $\epsilon_s = 12.5\,\epsilon_0$, $V_{bi} - V_{ext} = 2\,$V (small reverse bias), $N_D = 10^{16}\,$cm^{-3}, $T = 300\,$K. Charge distribution $\tilde{\rho}$ from (2.3) (*blue dashed line*) and $\rho = \rho(\tilde{\phi})$ from (2.2) (*red dashed line*). The *black dashed line* is the difference of the exact and approximate solution, $\Delta\tilde{\rho} = \rho_{exact} - \tilde{\rho}$.

The integral yields the electrical field analytically,

$$\tilde{E}(x) = \frac{\rho_0}{\epsilon_s}\left(x - L'_D \ln\left[\exp\left(w'/L'_D\right) + \exp\left(x/L'_D\right)\right]\right) . \tag{2.4}$$

The (maximum) field E_m at $x = 0$ is known analytically and leads to

$$w' = L'_D \ln\left(\exp\left[-\frac{\epsilon_s E_m}{L'_D \rho_0}\right] - 1\right) \approx L_D \sqrt{-2\,(\beta\,\phi_0 + 1)} . \tag{2.5}$$

The electrical field (2.4) can be analytically integrated to $\tilde{\phi}$ with the polylogarithm function [2] ($\xi_1 = \exp\left(x/L'_D\right)$, $\xi_2 = \exp\left(w'/L'_D\right)$),

$$\tilde{\phi} = -\frac{\rho_0}{\epsilon_s}\left(\frac{x^2}{2} + L'_D\,x\,(\ln[1 + \xi_1/\xi_2] - \ln[\xi_1 + \xi_2]) + L'^2_D\,\mathrm{Li}_2\,[-\xi_1/\xi_2]\right) . \tag{2.6}$$

The integration constant of the potential was chosen such that $\tilde{\phi}(x \to \infty) = 0$. The condition for the value of the potential at $x = 0$ yields the value of L'_D (for $w'/L'_D \gg 1$)

$$L'_D \approx \frac{\sqrt{6}}{\pi} L_D \approx 0.78\,L_D . \tag{2.7}$$

In Fig. 2.1 we compare the exact solution with this approximate solution. The charge distribution from the ansatz (2.3), using w' from (2.5) and L'_D from (2.7), is shown together with $\rho(\tilde{\phi})$ according to eq. (2.2). Ideally they should be the same. For our approximate solution (2.3), the two distributions are fairly close. The smooth transition around $x = w$ within about $\pm L_D$ is reproduced quite well. For our numerical example, the charge error between the exact and approximate solution, $\Delta\tilde{\rho} = \rho_{exact} - \tilde{\rho}$, is shown as blacked dashed line in Fig. 2.1 and has a maximum of about 5% of ρ_0.

[1] M. Grundmann, Space Charge Region Beyond the Abrupt Approximation, Phys. Status Solidi B 260(11), 2300257:1-4 (2023). doi:10.1002/pssb.202300257
[2] $\mathrm{Li}_n(x) = \sum_{k=1}^{\infty}(x^k/k^n)$; the polylogarithm of order $n = 2$ is also called dilogarithm.

2.2 Diffused oxygen as dominating shallow acceptor in p-type copper iodide thin films

M. Lorenz, P. Storm, S. Gierth*, S. Selle*, H. von Wenckstern, M. Grundmann

*Fraunhofer-Institut für Mikrostruktur von Werkstoffen und Systemen (IMWS) Halle

The long-term stability of the optically transparent p-type semiconductor copper iodide is a current challenge. We found the electrical conductivity of CuI thin films depending critically on the environmental impact. Al_2O_3 cappings enhance the stability considerably. Systematic studies on Al_2O_3/CuI heterostructures in dependence of the N_2/O_2 growth pressure show the electrical conductivity of the CuI films being determined by the oxygen diffusion through Al_2O_3 und CuI [1, 2]. Oxygen seems to be a dominating acceptor in CuI.

As an extension of the paper Ref. [1], we present here additional data which further illustrate the oxygen diffusion through Al_2O_3 capping layers into semiconducting CuI thin films [2].

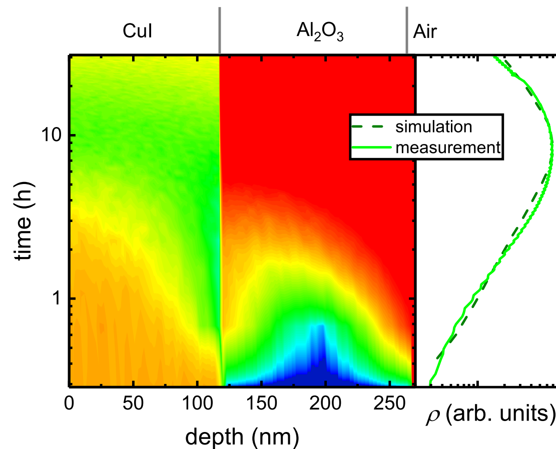

Figure 2.2: Time- and depth-resolved simulation of the diffusion-induced oxygen concentration in a c-sapphire/CuI + 1at% CuO/Al_2O_3 heterostructure in air [2]. The structure was grown in nitrogen gas at $p(N_2) = 5\times10^{-3}$ mbar. Blue stands for low, and red for high oxygen concentration. The Al_2O_3 capping layer is initially oxygen-depleted due to the growth in nitrogen. With increasing time, the capping layer saturates with oxygen (blue → red), partly at the expense of the oxygen from the CuI layer. The CuI layer is increasingly oxygen-depleted (orange → green), starting at the interface to Al_2O_3. On the right, the experimental resistivity ρ is shown together with the modeled curve [1, 2]. Figure taken from [2].

Figure 2.2 shows the simulation of the time- and depth-dependent oxygen diffusion in a c-sapphire/CuI + 1at% CuO/Al_2O_3 heterostructure in air (grown completely in nitrogen by Pulsed Laser Deposition PLD), corresponding to the diffusion regime assigned as R3 in Refs. [1, 2]. The depth 0 nm corresponds to the surface of the sapphire substrate, and the Al_2O_3 interface to the ambient air is approx. 260 nm total thickness. Figure 2.2 shows very impressively the depth-dependent oxygen diffusion from the CuI into the oxygen-depleted Al_2O_3, starting at the CuI/Al_2O_3 interface. With regard to

the resistivity ρ, the modeling based on the diffusion behavior reflects the experimental behavior very well (right in Fig. 2.2).

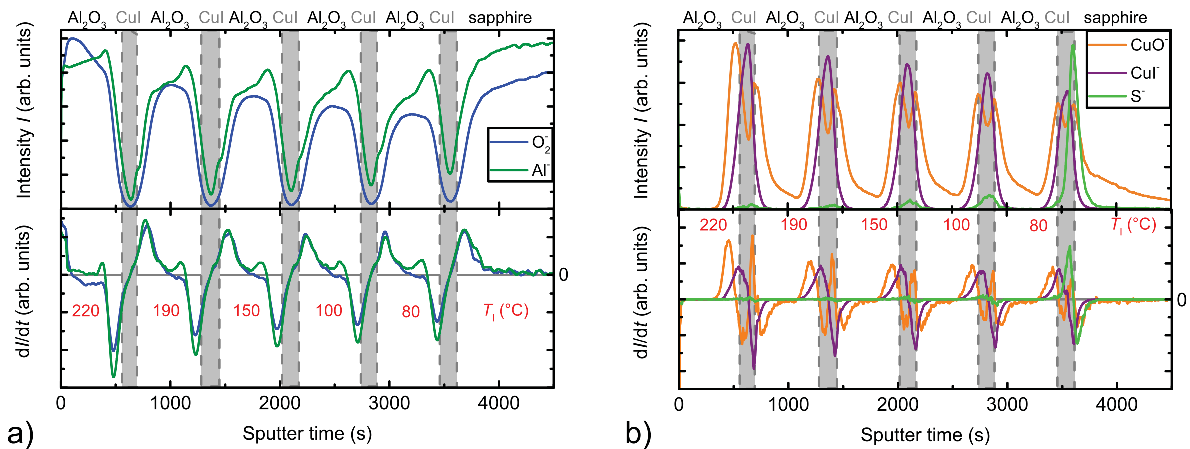

Figure 2.3: a), b) Depth-resolved ToF-SIMS signals (intensity I) with the derivatives dI/dt after the sputtering time t of a 5×(120 nm Al_2O_3/450 nm CuI) multilayer structure on c-sapphire, PLD grown with increasing growth temperatures of the individual bilayers inserted in red. a) shows the signals of O_2- and Al- from the Al_2O_3 films, and b) those of CuO-, CuI- and S- from the CuI films. All Al_2O_3 films in a) and b) were grown at $p(O_2) = 3\times10^{-3}$ mbar. Figures taken from [2].

Since the incorporation of impurities such as oxygen in CuI apparently strongly influences its electrical parameters, depth-resolved ToF-SIMS measurements were carried out to investigate the chemical composition of the CuI-Al_2O_3 heterostructures in detail. It should be noted that the individual ToF-SIMS signals can be strongly matrix-dependent. To minimize the number of depth profile measurements required, a special multilayer structure consisting of 5 bilayers of amorphous Al_2O_3 (thickness 120 nm) and CuI (thickness 450 nm) was grown on c-sapphire with PLD, with each bilayer grown at a different temperature, increasing from 80°C to 220°C, as denoted in Figure 2.3. This was to investigate the temperature effect on the chemical layer structure. The corresponding depth profiles for Al_2O3 and CuI are shown in Figures 2.3 a) and b). The exact separation of the Al_2O_3 and CuI layers in a) and b) was based on the depth values of half the maximum intensities of the CuI signals.

The Al- and O- signals in Fig. 2.3 a) are apparently not limited to the Al_2O_3 films, but extend into the CuI films, which is possibly due to the plasma dynamics during PLD growth. This penetration effect seems to increase with decreasing growth temperature. Regarding the CuI films, the CuI-, CuO- and S- signals can be seen in Figure 2.3 b). The CuI intensities show a much sharper demarcation to the Al_2O_3 layers compared to the Al and O profiles in a). The CuO- intensities are maximum at the interfaces to Al_2O_3, as expected. Consequently, copper at the interfaces is bound not only to iodine but also to oxygen. The CuO- signal also extends far into the Al_2O_3 layers and is clearly detectable through the entire layers, see Fig. 2.3 b). Since the exact determination of the oxygen content in the CuI layers is difficult due to the high oxygen presence in the covering layers, the sulfur signal S- was also recorded in Fig. 2.3 b). It is expected that sulphur also acts as a p-type dopant. The S- signal is visible in all 5 CuI films, with enrichment at the substrate-side interface. Since the S- intensity decreases with increasing growth

temperature (Fig. 2.3 b), we can assume thermal desorption for sulfur and thus probably also for oxygen in CuI [1, 2].

In summary, thin CuI films with top layers of Al_2O_3 were investigated with regard to the influence of the top layers on the electrical film parameters [1, 2]. Three different behaviors for uncovered CuI, for Al_2O_3 grown in oxygen, and for Al_2O_3 grown in nitrogen could be distinguished, for details see [1, 2]. We can explain the documented behavior with the oxygen diffusion between the CuI and Al_2O_3 layers and the atmosphere, see Figure 2.2. Oxygen acts as an acceptor in CuI, in agreement with theoretical calculations in [3]. The electrical activity of oxygen in CuI was also verified by intentional oxygen doping [1, 2]. The diffusion behavior of oxygen was further investigated by depth-resolved ToF-SIMS measurements. Traces of oxygen were found in the CuI films, and clear CuO signal peaks at the CuI-Al_2O_3 interfaces, see Figure 2.3.

Diffusion experiments with the 18O isotope support the previously determined effect of oxygen in CuI, see [1, 2]. Since the diffusion constant of oxygen in CuI determined here is significantly smaller than that calculated in Al_2O_3, the measured electrical conductivity of CuI seems to originate preferentially from a highly conductive charge carrier accumulation close to the interface and not from the entire CuI film thickness. The Hosono group in Japan has found similar oxygen-based effects of an ex-situ AlO_x passivation layer on textured CuI and CuI:Cs thin films in terms of hole concentration [4]. These results are significant for future applications of CuI in electronic devices, especially for film growth and device design when non-degenerate films with moderate hole concentration are required.

We have to thank the German Research Foundation DFG for financial support within the research group FOR 2857, subprojects P01 (LO790/7-1) and P05 (WE4620/5-1). We would also like to thank Michael S. Bar, Monika Hahn, Holger Hochmuth, René Feder, Vanesa Núnez and Alexander Kemptner for a wide range of experimental support for this work. The University of Leipzig supports the work in the research profile area "Complex Matter".

[1] P. Storm, S. Gierth, S. Selle, M.S. Bar, H. von Wenckstern, M. Grundmann, M. Lorenz, APL Mater. 2021, **9** (5), 051101, doi:10.1063/5.0047723.

[2] M. Lorenz, P. torm, S. Gierth, S. Selle, H. von Wenckstern, M. Grundmann, Chem. Ing. Tech. 2023, **95** (11), 1786-1793, doi:10.1002/cite.202300007.

[3] M. Grauzinyte, S. Botti, M.A.L. Marques, S. Goedecker, J.A. Flores-Livas, Phys. Chem. Chem. Phys. 2019, **21** (35), 18839-18849, doi:10.1039/C9CP02711D.

[4] K. Matsuzaki, N. Tsunoda, Y. Kumagai, Y. Tang, K. Nomura, F. Oba, H. Hosono, J. Am. Chem. Soc. 2022, **144** (36), 16572-16578, doi:10.1021/jacs.2c06283.

2.3 Heteroepitaxial (00.1) Mn^{2+}-Doped Zn_2GeO_4 Green-Emitting Phosphor Thin Films Grown on C-Plane Sapphire

S. Luo, L. Trefflich

We report the heteroepitaxial growth of (00.1)-oriented Mn2+-doped Zn2GeO4 thin films on c-plane sapphire substrates using pulsed laser deposition. The 400 nm thick

film shows a surface RMS roughness of about 1.2 nm, and exhibit a full width at half maximum (FWHM) of rocking curve of (00.6) reflex of about 0.18°. The steady-state photoluminescence (PL) spectra of film under 266 nm laser excitation at room temperature exhibit a narrow green emission band centered at 541 nm with a FWHM of 47 nm, which originates from the $^4T_1 \rightarrow {}^6A_1$ transition of Mn^{2+} that substituted Zn^{2+} in the Zn_2GeO_4 host. This work opens a way to the fundamental study on epitaxial Mn-doped Zn_2GeO_4 green-emitting phosphor thin films for potential device application.

Ultrawide bandgap willemite-type Zn_2GeO_4 with a bandgap of about 4.9 eV, becoming green phosphors through Mn^{2+} doping in the form of polycrystalline films and powders, have been attracting great interests in the past two decades for potential applications in displays, solid-state lighting, bioluminescence, anticounterfeiting and fingerprint detection. However, the abundant defects that are not avoid in the polycrystalline films and powders inevitably cause additional defect-state emission and multiple emission bands, which have been a significantly challenging for fundamental research in view of potential device application. Due to the lack of bulk single crystal for experimental investigation, the epitaxial thin films of Mn-doped Zn_2GeO_4 grown on commercially available single crystal substrates are preferable to the fundamental study on their physical and chemical properties for practical device application, especially in film-based devices. In our previous work, we reported the epitaxial (00.1) Zn_2GeO_4 thin films grown on c-plane sapphire substrates by pulsed laser deposition (PLD) using a Zn-rich target with the Zn:Ge atomic ratio of about 4:1, whereas the resulting films exhibiting apparently Zn interstitial-related photoluminescence (PL). Here we report the heteroepitaxial growth of (00.1)-oriented Mn^{2+}-doped Zn_2GeO_4 thin film on c-plane sapphire (c-sapphire) substrate by PLD. In order to avoid the addition of Zn interstitial into the films, the content of ZnO was reduced in the target. In this work, two homogeneous bulk targets for PLD were fabricated through a two-step sintering process using the mixed raw powders of 35 wt. % GeO_2 and 65 wt. % ZnO for undoped target, and 35 wt. % GeO_2, 64 wt. % ZnO and 1 wt. % MnO for Mn-doped target, respectively. The atomic ratios of Zn: Ge and Mn: Zn: Ge are approximately 2.39:1 and 0.042:2.35:1 for the two targets, respectively. A 248 nm KrF excimer laser was used for PLD with a 5 Hz repetition, and the laser fluence on target surface is about 5 J/cm^2. The setting temperature for deposition is about 800°C. Spectroscopic ellipsometery (SE) measurements were performed at room temperature to evaluate the film thickness using a J. A. Woollam CR2 spectroscopic ellipsometer.

Figure 2.4(a) shows the XRD patterns of the undoped thin films deposited with 18000 pulses under different oxygen partial pressures of 0.01, 0.05, 0.10 and 0.20 mbar. The 2Θ-ω scans were aligned with calibration using (00.6) α-Al_2O_3 reflection at 41.700°(c=12.980 Å. It is clearly observed that the films deposited under 0.01, 0.05 and 0.10 mbar oxygen pressure exhibit only one peak corresponding to (00.6) reflection of willemite-type hexagonal Zn_2GeO_4. Figure 2.4(b) shows the rocking curve of (00.6) peak of the films deposited under different oxygen pressures. The full width at half maximum (FWHM) of rocking curve of (00.6) Zn_2GeO_4 peak is about 0.42°, 0.38°and 0.23°for the films deposited under 0.01, 0.05 and 0.10 mbar pressure with a film thickness of about 700 nm, 500 nm and 350 nm, respectively. It is suggested that the 0.10 mbar oxygen partial pressure is optimal for obtaining high-quality thin film. As shown in Fig. 2.4(c), the phi scan results show that six peaks with 60-degree intervals of the Zn_2GeO_4 thin films are aligned with respect to the six peaks of the c-sapphire substrate, confirming an

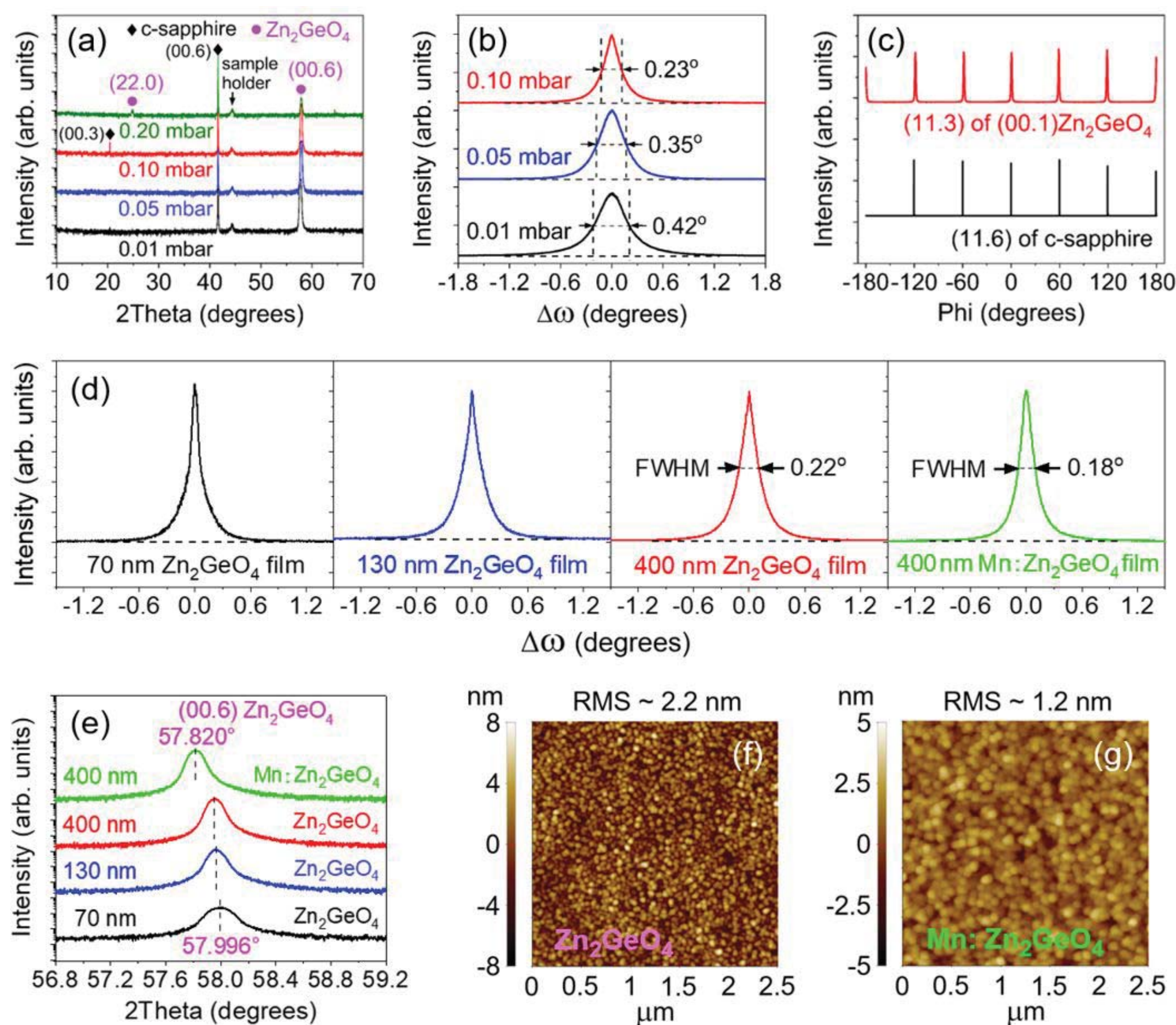

Figure 2.4: (a) XRD 2theta-omega scans of undoped thin films deposited under different oxygen partial pressures. (b) Rocking curves of (00.6) peak of undoped thin films deposited under different oxygen pressures of 0.01, 0.05 and 0.10 mbar. (c) Phi scans of (11.3) and (11.6) for the (00.1)-oriented thin film and the c-sapphire substrates, respectively. (d) Rocking curves of (00.6) peak of undoped and Mn-doped epitaxial thin films with the indicated thickness deposited under 0.01 mbar oxygen pressures. (e) Selected (00.6) peaks of XRD patterns of the films. AFM surface morphologies of (f) undoped and (g) Mn-doped (00.1) Zn2GeO4 epitaxial thin films with a thickness of about 400 nm.

in-plane epitaxial matching between the (00.1) crystal plane of Zn_2GeO_4 thin films and the (00.1) crystal plane of c-sapphire substrate. The in-plane orientation relationships are identified to be [10.0] Zn_2GeO_4 // [10.0] Al_2O_3 and [11.0] Zn_2GeO_4 // [11.0] Al_2O_3. The rocking curves of (00.6) peak of undoped and Mn-doped epitaxial thin films with different thicknesses deposited under 0.10 mbar oxygen pressure are shown in Fig. 2.4(d). The rocking curves of the 70 nm and 130 nm thick films are a superposition of a broad bottom peak with a narrow top peak, while the 400 nm thick film shows one-component shape of rocking curve. The 400 nm thick undoped and Mn-doped films exhibit a FWHM of rocking curve of (00.6) reflex of about 0.22°and 0.18°, respectively. The selected (00.6) reflexes of XRD patterns of the thin films are shown in Fig. 2.4(e). A

slight shift to smaller angles for the (00.6) peak is observed as the thickness increases for the undoped films. The calculated c-lattice constant of the 70 nm and 400 nm thick undoped films, according to the 2Θ values of 57.996°and 57.955°for the (00.6) Zn_2GeO_4 reflection, is approximately 9.534 Å and 9.540 Å, respectively. These results are in line with the experimental value range from 9.507 Å (powder) to 9.547 Å (single crystal), indicating no significant strain present in the films. Whereas the 400 nm thick Mn-doped film shows an apparently greater value of c lattice constant of about 9.560 Å, indicating a significant doping of Mn ions in the Zn_2GeO_4 host. From the AFM surface morphologies of 400 nm thick undoped and Mn-doped films, as shown in Fig. 2.4(f-g), it is clearly observed that the Mn-doped epitaxial thin film exhibits a larger grain size and a smoother surface.

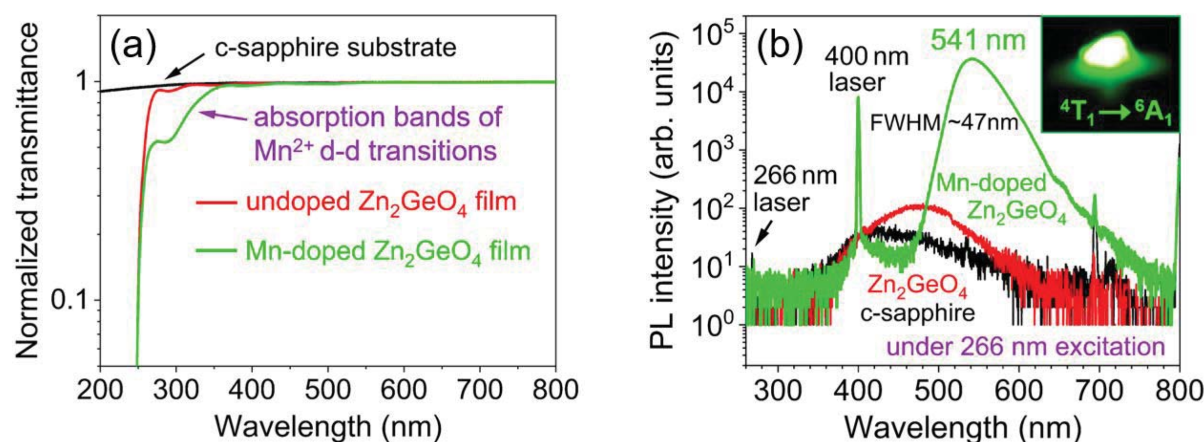

Figure 2.5: (a) UV-visible transmission spectra of the undoped and Mn-doped (00.1) Zn_2GeO_4 epitaxial thin films grown on c-sapphire substrates. (b) Steady-state photoluminescence (PL) spectra of the Mn_2+-doped (00.1) Zn_2GeO_4 epitaxial thin films under 266 nm excitation at room temperature. The inset is a photo showing the bright green emitting of Mn_2+-doped thin film in a dark room.

The optical transmission of 400 nm thick undoped and Mn-doped epitaxial thin films were measured by using a Perkin-Elmer Lambda 19 UV/Vis/NIR spectrophotometer at room temperature. Figure 2.5(a) presents the UV-visible transmission spectra of thin films, showing the sharp optical absorption edges ending at about 245 nm. The broad absorption band of around 270~360 nm for Mn-doped film is attributed to the band-to-band transitions of Mn cations. The steady-state photoluminescence (PL) experiments were performed at room temperature with a custom-build micro-PL setup under pulsed laser excitation at 266 nm and using a Horiba iHR 320 spectrometer. A Coherent Mira HP Ti:Sapphire femtosecond laser with a repetition rate of 76 MHz and a pulse length of 200 fs was used for the steady-state PL measurements. Figure 2.5(b) shows the room-temperature steady-state PL emission spectra of the undoped and Mn-doped (00.1) Zn_2GeO_4 epitaxial thin films with a thickness of about 400 nm deposited under 0.1 mbar oxygen pressure. A narrow band of green emission was observed, as very bright visible as shown in the inserted photo taken in the dark room, at 541 nm with a FWHM of about 47 nm. Apparently, it is an emission band from $^4T_1 \rightarrow {}^6A_1$ transition of Mn_{2+} that substituted Zn_{2+} in the Zn_2GeO_4 host. It is well-known that a spectrally narrow, i.e., 25-60 nm in FWHM, green emission peaked at 500-550 nm originates from the lowest

$^4T_1 \rightarrow {}^6A_1$ transition of Mn2+ occupied center site of tetrahedral crystal field. In the case of this study, the Mn2+ ions substituted Zn_{2+} ions and occupy the center site of tetrahedral crystal field in the willemite-type Zn_2GeO_4 host.

2.4 Exploration of Zr doping in pulsed laser deposited α-Ga_2O_3 for device applications

S. Vogt, T. Schultz, C. Petersen, H. von Wenckstern, N. Koch and M. Grundmann

The material Ga_2O_3 is of great interest for high power devices due to its high expected breakdown field. For the thermodynamically stable β-phase of Ga_2O_3, a breakdown field as high as 8 MV/cm is expected[1–3]. However, crystalline β-Ga_2O_3 substrates are required for optimal device performance. In contrast, highly crystalline α-Ga_2O_3 thin films can be grown on isostructural, cost-efficient and readily available α-Al_2O_3 substrates. Furthermore, the α-phase has a larger bandgap than the β-phase and even higher breakdown fields of up to 10 MV/cm are expected. The growth of α-Ga_2O_3 thin films has been demonstrated with different growth techniques, such as mist chemical vapor deposition (CVD) [4–6], molecular beam epitaxy (MBE) [7] and pulsed laser deposition (PLD) [8–10]. In order to tailor the electrical properties for specific device applications, silicon and tin are commonly investigated as shallow donors for α-Ga_2O_3 [11, 12]. However, also germanium doping has yielded promising results[14, 15]. The investigation of further dopants is particularly interesting if doping of the α-$(Al_xGa_{1-x})_2O_3$ alloy is considered. Calculations by Wickramaratne *et al.* indicate different critical alumnium concentrations x, at which the donors do not act as donors anymore[16]. The most promising donors for this alloy are silicon, hafnium and zirconium. However, hafnium and zirconium doping of α-Ga_2O_3 have not yet been demonstrated.

In this work we demonstrate the suitability of zirconium doping of α-Ga_2O_3. For that, targets with different amounts of zirconium, ranging from 0.001 wt.% to 1 wt.%, were fabricated to tune the electrical properties. All thin films were deposited on m-plane sapphire in a two step process by pulsed laser deposition (PLD) [14]. For the doped layer, the growth temperature was varied between 375°C and 550°C. The crystallization in the alpha phase was confirmed for all thin films by X-ray diffraction. For all doping concentrations, a strong dependency of the resistivity on the growth temperature was observed. For small as well as for high growth temperatures, an increase of the resistivity was observed. X-ray photoelectron spectroscopy measurements were used to investigate the zirconium incorporation in the thin film for different growth temperatures. A depletion of zirconium towards the sample surface is observed, which can be prevented by the in-situ growth of an Al_2O_3 capping layer. Furthermore, the growth temperature strongly influences the amount of zirconium in the thin films. For higher growth temperatures, an increased desorption of volatile GaO_2 sub-oxides occurs during the thin film growth, leading to higher zirconium contents for a given target. Highly conductive thin films with a resistivity as low as $3.3 \times 10^{-3}\ \Omega$cm were achieved at carrier densities as high as 5.8×10^{19} cm^{-3}.

On two suitable thin films, Schottky barrier diodes were realized with PtO_x/Pt for the Schottky contact and Ti/Al/Au as ohmic contact. The diodes have high current rectification ratios of up to 8.5 orders of magnitude and homogeneous barrier height

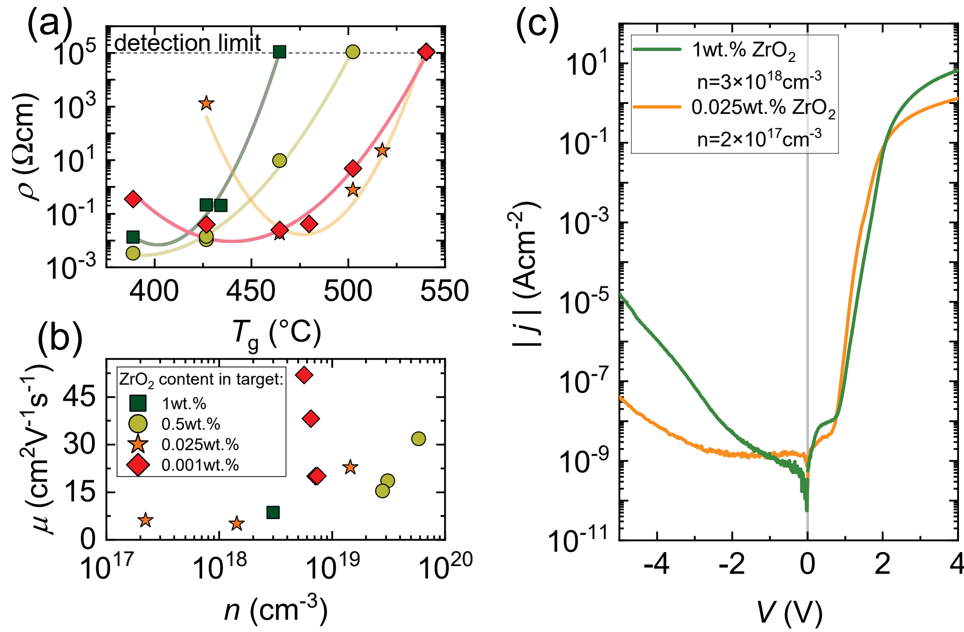

Figure 2.6: (a) Resistivity ρ as a function of the growth temperature for four targets with zirconium contents between 0.001 wt.% and 1 wt.% and (b) the electron mobility μ in dependence on the free carrier density *n* determined by Hall effect measurements for thin films grown from targets with different compositions and at different growth temperatures. In (c) exemplary current density-voltage characteristics of two diodes with a PtO_x/Pt gate Schottky barrier contact fabricated on two thin films deposited from different targets as denoted.

of 1.4 eV at room temperature. A detailed description of these results was published in [17].

[1] A. Hassa *et al.*: J. Phys. D: Appl. Phys. **54**, 223001 (2021)
[2] J. Zhang *et al.*: APL Mater. **8**, 010906 (2020)
[3] M. Higashiwaki *et al.*: Semicond. Sci. Technol. **31** 034001 (2016)
[4] S. Fujita *et al.*: J. Cryst. Growth **401**, 588-592 (2014)
[5] K. Kaneko *et al.*: J. Cryst. Growth **436**, 150-154 (2016)
[6] G. Dang *et al.*: Appl. Phys. Lett. **113**, 062102 (2018)
[7] R. Kumaran *et al.*: Opt. Lett. **35**, 3793 (2010)
[8] M. Lorenz *et al.*: Appl. Phys. Lett. **113**, 231902 (2018)
[9] M. Grundmann *et al.*: APL Mater. **8**, 021108 (2020)
[10] A. Hassa *et al.*: phys. stat. sol. (b) **258**, 2000394 (2020)
[11] T. Uchida *et al.*: MRS Advances **3**, 171-177 (2018)
[12] K. Akaiwa *et al.*: Jpn. J. Appl. Phys. **55**, 1202BA (2016)
[13] M. Kneiß *et al.*: APL Mater. **7**, 022516 (2019)
[14] S. Vogt *et al.*: Phys. Status Solidi A **220**(3), 2200721:1-6 (2023)
[15] T. Wakamatsu *et al.*: J. Appl. Phys. **135**, 155705 (2024)
[16] D. Wickramaratne *et al.*: Appl. Phys. Lett. **121**(4), 042110 (2022)
[17] S. Vogt *et al.*: Phys. Rev. Appl. (accepted), (2024)

2.5 Demonstration of Two Multi-component Target Ablation Approaches and Their Application in Pulsed Laser Deposition

A. Jörns, H. von Wenckstern, S. Vogt, P. Schlupp, M. Grundmann

Combinatorial pulsed laser deposition (C-PLD) gives a solid foundation for high-throughput screening methods used for rapid discovery of novel advanced materials. One promising approach is utilizing segmented targets for systematically tuning elemental composition and therefore material properties. Since target exchange during deposition is not required, deposition time and material consumption is significantly reduced compared to conventional PLD approaches. However, fabrication of established segmented targets may be challenging or not even possible for certian material combinations. In this work, we propose two different C-PLD approaches based on easy-to-fabricate segmented targets [1].

The first approach is an adaptation of a PLD variant introduced by Christen *et al.* where the stoichiometry of volatile potassium in $KTa_{1-x}Nb_xO_3$ was controlled by an azimuthally segmented target approach [2]. In our work, we used a target consisting of two semi-circular segments of material A and B. During deposition the target is rotated and simultaneously moved vertically resulting with a fixed laser spot in a circular ablation area. By introducing a lateral shift δ of the target rotation axis from the target center the ratio of the ablation area on the respective segment and thus the resulting thin film composition can be adjusted. In the following, this approach is denoted as ORA (Off-centered Rotation Axis) PLD. The second approach is a new target segmentation design defined by an ABA-structure (referred to as ABA-PLD) where B is a horizontal bar between two semi-circular segments of A. In this case, the target is also rotated during deposition, but the vertical position of the target is fixed resulting in a ring-shaped ablation track. The composition can be adjusted by changing the vertical position of the target, *i.e.* the radius R of the laser track. A schematic for both approaches is depicted in Fig. 2.7.

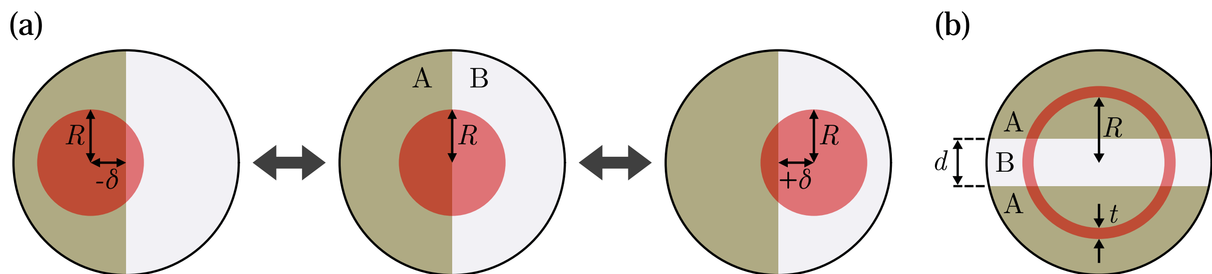

Figure 2.7: a) Azimuthally segmented target with segment materials A and B for three different offsets of center of rotation δ at fixed radius R of laser ablation area. b) ABA-segmented target with horizontal cuboid of width d and with ring-shaped laser ablation area of radius R and width t

By calculating the overlap between laser ablation area and each target segment, the material composition of a deposited thin film can be determined without considering the details of plasma formation, plume propagation, nucleation and film growth. Since

this calculation assumes a priori the same ablation rate for both segment materials, a weighting factor was introduced taking into account the real material transfer rates. Simulations were made showing the effect of this factor and the different geometric parameters used in Fig. 2.7 on composition.

As proof-of-concept, the techniques were employed on the transparent, semiconducting ternary alloy zinc-tin-oxide. A series of samples were fabricated using each novel approach and subsequently investigated in terms of structural, morphological and electrical properties. Fig. 2.8 depicts the zinc cation content x of $Zn_xSn_{1-x}O$ measured by energy-dispersive X-ray spectroscopy (EDX) for samples deposited by the two approaches. Simulations made beforehand are in excellent agreement with the experimental data. Each approach allows to cover the entire phase diagram (with the ABA-segmentation an inverse target is additionally required). All samples with mixed composition of zinc and tin are X-ray amorphous with surface roughness of below 4 nm. Charge carrier concentration can be tuned with composition in the range $n \approx 10^{15} - 10^{20}\,\mathrm{cm}^{-3}$ and is lowest for $x \approx 0.75$. On all samples prepared by these methods droplets, originating from the cutting edge, are present, which can be drastically reduced by frequent grinding and polishing of the target surface.

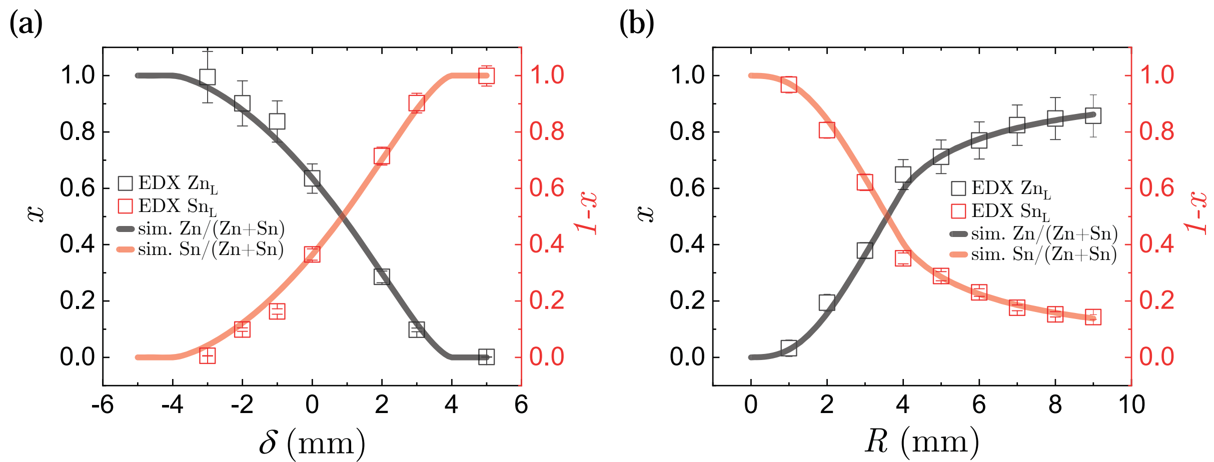

Figure 2.8: EDX measurements of samples prepared by using a) the AB-segmented target with rotation offset and b) ABA target segmentation. Solid lines show simulated Zn and Sn cation contents in a) for $R = 4$ mm in dependence on the rotation axis offset δ and in b) for $d = 6$ mm, $t = 2$ mm in dependence on the radial laser offset R. For both methods a weighting factor of $\gamma_{ZnO}/\gamma_{SnO_2} = 1.75$ was applied

Both demonstrated methods can be used to create discrete composition material libraries and vertical composition gradients by in-situ controlling the rotation offset or the laser track radius, respectively. Since the simulations showed excellent agreement with the experimental data, these approaches can be used to predict the composition for designated target and deposition parameters and thus thin films with specific composition can be fabricated in a targeted manner on demand.

[1] A. Jörns, H. von Wenckstern, S. Vogt, P. Schlupp, and M. Grundmann, Adv. Phys. Res. 2300140(2024). /doi10.1002/apxr.202300140
[2] H.-M. Christen *et al.*, Thin Solid Films, **312**, 156-159 (1998).

2.6 Oxygen Plasma Treatment to Enable Indium Oxide MESFET Devices

F. Schöppach D. Splith, M. Grundmann, H. von Wenckstern

Wide bandgap semiconductors have applications as transparent electrodes and potentially as active materials in transparent electronics. Within this class of materials, indium oxide stands out for its exceptionally high electron mobility. However, the realization of active devices based on In_2O_3 is non-trivial, mainly due to the difficulties in realizing rectifying Schottky barrier diodes. We present a systematic study of the beneficial effect of remote oxygen plasma treatments on the performance of metal-semiconductor field-effect transistors (MESFETs). The In_2O_3:Mg thin films were grown by pulsed laser deposition on r-plane sapphire substrates at about 500°C. Magnesium is a compensating acceptor in In_2O_3 and is used to adjust the free electron concentration (fec) of the functional layers. Three different sample series with Mg contents of 0%, 1.2% and 2.3% are investigated and compared for different layer thicknesses. In general, the resistivity of the layers increases by about 2 and 5 orders of magnitude with increasing Mg concentration in the as-grown state. After exposing the samples to argon and oxygen plasma treatment, respectively, the electrical transport properties were re-examined. For undoped films, the conductivity increases by a factor of ten after Ar plasma treatment due to an increase in fec. Oxygen plasma exposure leaves the transport properties unchanged. For the Mg-doped samples, the conductivity increases significantly, especially for Ar plasma treatment, after which the sample properties are similar to those of undoped layers. The variation of the layer resistivity and fec with thickness of the plasma-treated samples shows that the electrical transport is restricted to a region near the surface, called the surface electron accumulation layer (SEAL), caused by shallow defects created during the plasma treatment [1]. The formation of the SEAL can be avoided by a gentle remote plasma cleaning process using process parameters that result in lower kinetic energies of the plasma species suppressing process-induced defect formation [1]. This is demonstrated by studying the properties of Schottky barrier diodes (SBDs) as a function of plasma process parameters. For doped and undoped samples, the properties of SBDs depend critically on the process parameters. No rectification is achieved with Ar plasma treatment. Oxygen plasma treatment yields rectifying SBDs with best performance at low plasma density. Optimized parameters allow the reproducible fabrication of SBDs with six orders of magnitude in current rectification, an effective barrier height of 0.9 eV and an ideality factor below 1.5. In a next step, In_2O_3 and In_2O_3:Mg based MESFETs were fabricated. Figure 2.9 shows the transfer characteristics of typical transistors for different sample states. We compare MESFETs from untreated and remote oxygen plasma treated devices. Plasma treatment was applied i) before, ii) after, and iii) before and after gate contact deposition, respectively. The best device performance was found for Mg-doped thin films and transistors with oxygen plasma treatment after gate contact deposition. Such devices have current swing of more than six orders of magnitude and subthreshold swing of 120 mV. As shown in Fig. 2.9, the off-current is reduced by about three orders of magnitude by the post-gate plasma process. In contrast to SBDs, remote oxygen plasma treatment prior to deposition of the Schottky contact metal does not improve the FET characteristics. The combination of pre- and post-gate plasma exposure is only benefi-

cial for FETs on undoped In_2O_3 layers, while an exclusive post-gate plasma treatment gives the best properties for FETs on Mg-doped In_2O_3 [1].

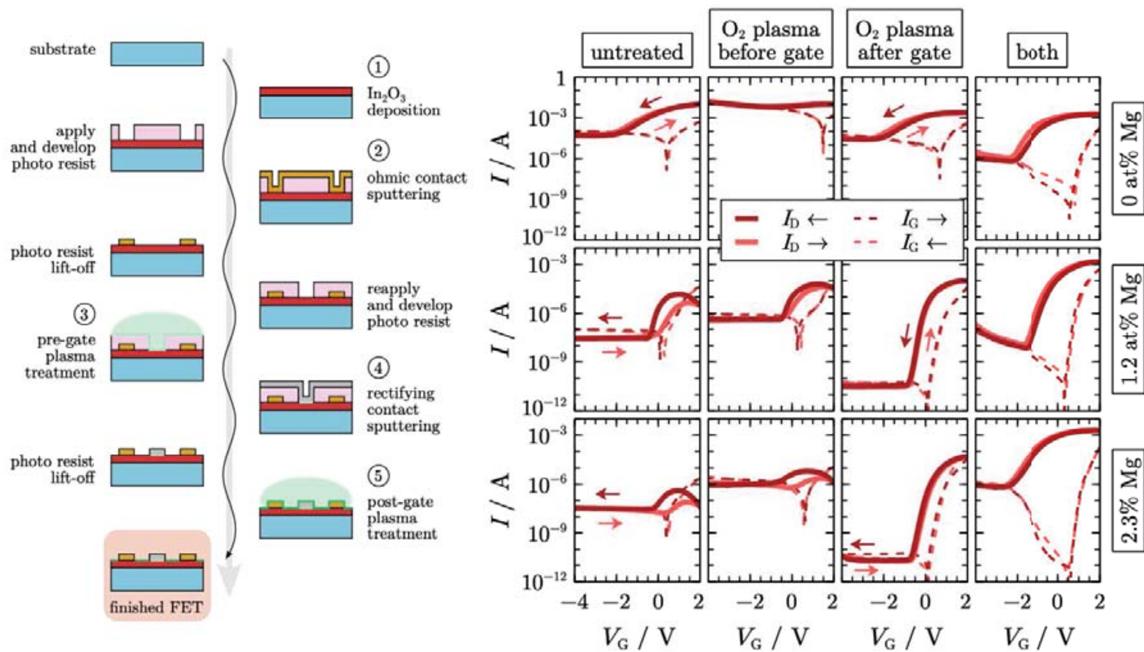

Figure 2.9: Work flow of MESFET fabrication with optional plasma treatment steps 3 and 5. Transfer characteristics of typical devices are depicted for doped and undoped In_2O_3 thin films for plasma processes as labeled

[1] F. Schöppach, D. Splith, M. Grundmann and H. von Wenckstern, Adv. Electron. Mater. **2023**, 9, 2300291 (2023).

2.7 Growth of κ-$([Al,In]_xGa_{1-x})_2O_3$ Quantum Wells and Their Potential for Quantum-Well Infrared Photodetectors

H. von Wenckstern, T. Schultz*, M. Kneiß, P. Sturm, D. Splith, N. Koch*, A. Hammud*, M. Grundmann

*Humboldt Universität zu Berlin, Institut für Physik, Brook-Taylor-Straße 6, 12489 Berlin

Due to the wide range of miscibility, κ-$([Al,In]_xGa_{1-x})_2O_3$ is particularly suitable for bandgap engineering in the large range from about 4 eV to 6 eV [1]. This makes the material promising for heterostructure-based applications such as high electron mobility transistors and quantum well infrared photodetectors (QWIP). The latter are advantageous over existing solutions because they combine high sensitivity in the infrared (IR) with transparency in the visible and UV spectral regions, enabling low-noise IR detectors. We investigate quantum well thin film heterostructures realized by

combinatorial pulsed laser deposition experimentally by X-ray diffraction (XRD), depth resolved X-ray photoelectron spectroscopy (XPS) and transmission electron microscopy (TEM) as well as by quantum well simulations based on the self-consistent solution of the Poisson and Schrödinger equation [2]. We focus on the one hand on the realization and experimental investigation of quantum well structures with well-defined layer thicknesses and on the other hand the potential spectral range that can be covered within the κ-$([Al,In]_xGa_{1-x})_2O_3$ material system.

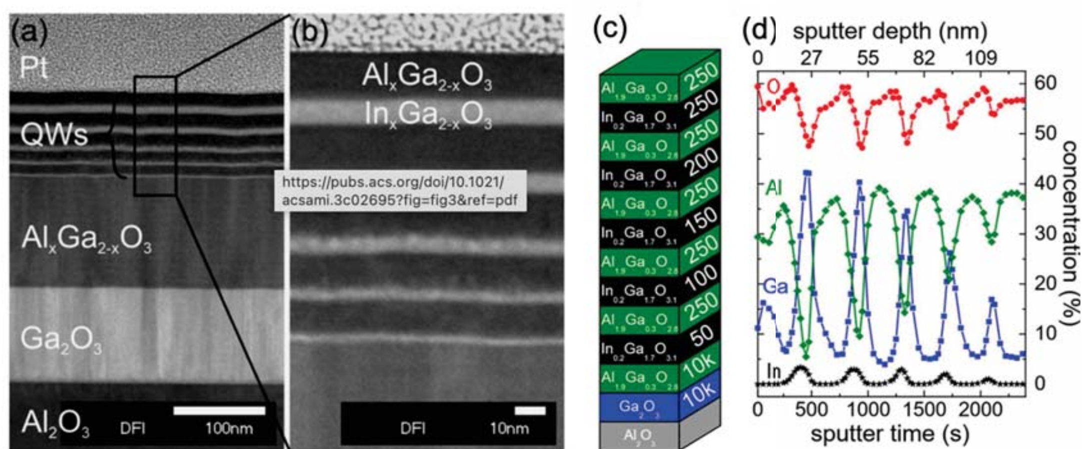

Figure 2.10: (a) Overview TEM image of the cross section of the entire sample stack. (b) Zoom into the QW region indicated by the black rectangle in (a), used quantification of the QW thicknesses. (c) Schematic sample structure. The numbers indicate the number of laser pulses used for the individual layer deposition. (d) XPS depth profile of the multi-QW sample illustrated in (a)-(c). The sputter time was converted to a sputter depth by calibrating the total sputter depth with a DEKTAK profilometer measurement

The sample structure used for the experimental investigations is shown in Fig. 2.10(c). First, a binary κ-$Ga_{1-x2}O_3$ buffer layer is deposited on a c-plane sapphire substrate. The κ-$([Al,In]_xGa_{1-x})_2O_3$ quantum well stack is then deposited with varying thicknesses of the indium-containing quantum well layers. The layer thickness was precisely determined from the TEM studies shown in Fig. 2.10 (a,b). From these data, a linear relationship was established between the number of laser pulses n used and the resulting thickness d of the quantum wells: $d = 0.033\,\text{nm} \times n$. An XPS depth profile was recorded by Ar ion etching with a minimum available ion energy of 300 eV to minimize sputtering damage between repeated XPS measurements. We show that accurate modeling yields quantum well layer thicknesses in agreement with TEM results. The modeling must account for the inelastic mean free path of the emitted photoelectrons as well as the signal broadening induced by the sputtering process. This is especially important for quantum well layer thicknesses below 5 nm. Our simulations of the transition energy of quantum well structures show that the spectral onset of QWIP detectors can be tuned from about 1 to 100 μm in the κ-$([Al,In]_xGa_{1-x})_2O_3$ material system. This underlines its particular suitability for the realization of next-generation low-noise QWIP photodetectors [2].

[1] A. Hassa, M. Grundmann, H. von Wenckstern, J. Phys. D: Appl. Phys. **54**, 223001 (2021).

[2] T. Schultz, M. Kneiß, P. Storm, D. Splith, H. von Wenckstern, C. T. Koch, A. Hammud, M. Grundmann, and N. Koch, ACS Appl. Mater. Interfaces **15**, 24, 29535–29541 (2023).

2.8 Defect level in κ-Ga_2O_3 revealed by thermal admittance spectroscopy

A. Langørgen*, Y.K. Frodason*, R. Karsthof*, I.J. ThueJensen*, L. Vines*, M. Grundmann, H. von Wenckstern

*Department of Physics and Centre for Materials Science and Nanotechnology

Ga_2O_3 is emerging as a viable alternative to GaN or SiC for the fabrication of high-power electronic devices. It appears in various polymorphs among which the monoclinic β-gallia structure is thermodynamically most stable [1]. Besides, orthorhombic κ-Ga_2O_3 is promising for high-power devices and high electron mobility transistors due to its predicted large value of its spontaneous polarization. However, the avaialbe literature on material properties and particularly on charge transition levels of dopants and defects in this polymorph is very limited. We report results of first-principles calculations as well as of thermal admittance spectroscopy (TAS) and secondary ion mass spectroscopy (SIMS) of a κ-Ga_2O_3 thin film grown by tin-assisted pulsed laser deposition [2]. Schottky barrier contacts, required for the TAS investigation, were realized by reactive sputtering of platinum. These diodes have a high current rectification of about eight orders of magnitude for best contacts and a net doping density of about 2×10^{18}cm^{-3}. We found one defect state with concentration of about 3×10^{17}cm^{-3}, thermal activation energy of about 210 meV and an apparent capture cross-section of 3×10^{-16} cm^2. The SIMS measurements reveal a tin concentration of about 6×10^{19} cm^{-3} which is caused by the tin-assisted growth, and impurity concentrations of Si and Fe of 2×10^{18} and 1×10^{18}cm^{-3}, respectively.

First-principles calculations were performed to investigate the microscopic origin of the defect level observed in TAS. We considered the incorporation of Si, Sn and Fe at the four different cation sites of the orthorhombic Ga_2O_3. Si behaves as shallow donor and is not a candidate for the trap level. Iron on Ga-site forms a deep acceptor state and is therefore not responsible for the defect state. Further, incorporation of tin on the Ga2, Ga3 and Ga4 site results in a shallow defect state. Tin substitutung the fourfould coordinated Ga1 yields a defect state with charge transition level of 0.24 eV below the conduction band minimum, very close to the experimental value of 0.21 eV [2]. Thus, the origin of the observed defect level is tentatively assigned to Sn_{Ga1} [2].

[1] H. von Wenckstern, Adv. Electron. Mater. **3**, 1600350 (2017).
[2] A. Langørgen, Y. K. Frodason, R. Karsthof, H. von Wenckstern, I. J. Thue Jensen, L. Vines, M. Grundmann, J. Appl. Phys. **134**, 015701 (2023).

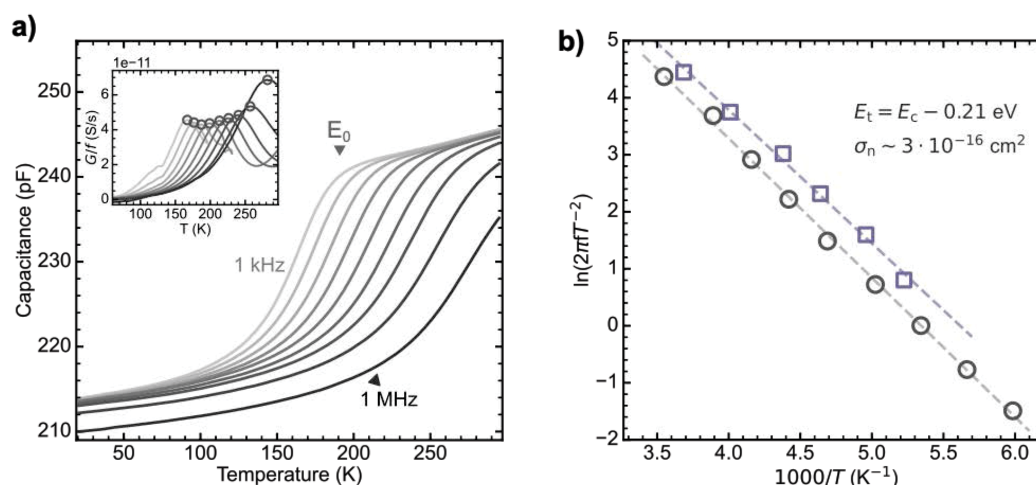

Figure 2.11: a) Temperature dependence of the capacitance of the Pt/κ-Ga_2O_3 Schottky barrier diode for frequencies between 1 kHz and 1 MHz. The inset shows the frequency normalized conductance with markers indicating positions of maxima used to construct the Arrhenius plot shown in b)

2.9 Cation segregation observed in an $(In,Ga)_2O_3$ material thin film library beyond the miscibility limit of the bixbyite structure

S. Montag, D. Splith, M. Kneiß, M. Grundmann, J. GarciaFernandez*, Ø. Prytz*, H. von Wenckstern,

*Department of Physics and Centre for Materials Science and Nanotechnology

The miscibility of In_2O_3 and Ga_2O_3 is investigated [2]. The structural and optical properties of ternary thin films of a discrete composition spread material library, created using combinatorial pulsed laser deposion [1], are determined as a function of cation composition. In_2O_3 and Ga_2O_3 are wide bandgap semiconductors with potential applications as rectifiers, transistors and detectors [3]. They crystallize in the cubic bixbyite and monoclinic beta-gallium structure, respectively. Therefore, a miscibility gap will exist. For the incorporation of In_2O_3 into monoclinic Ga_2O_3, phase separation is reported for indium cation contents above 40%. The incorporation of Ga_2O_3 into cubic In_2O_3 leads to a decrease of the lattice constant and an increase of the aborption edge. We observe a linear decrease of the lattice constant which is well described by Vegard's law: $a(x) = a(0) + (1 - x)a(1)$ with $a(0) = 10.119$ Å and $a(1) = 9.043$ Å for $x < 0.2$. For larger Ga contents the lattice constant saturates at a value of about 9.95 Å, indicating the miscibility limit. Correspondingly, the aborption edge energy $E_{g,opt}$ increases with increasing Ga content for $x < 0.2$ and saturates at about 3.85 eV for higher Ga contents. A linear fit of the data gives $E_{g,opt} = 3.75\,\mathrm{eV} + 0.517\,\mathrm{eV} \times x$. The composition and microstructure of three selected samples with $x = 0.11$, 0.22 and 0.35 were examined by transmission electron microscopy. The sample with Ga content below the miscibility limit at $x = 0.11$ shows a homogeneous phase and distribution of cations. It consists of columnar grains with a length of 150 to 300 nm and a width of 30 to 70 nm [2]. The

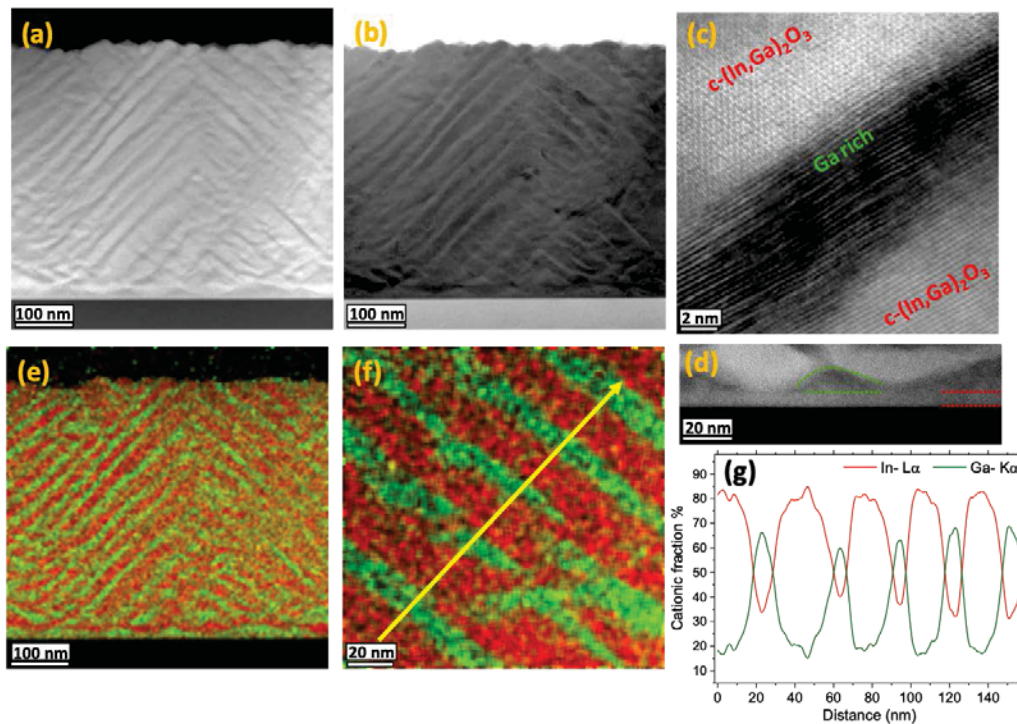

Figure 2.12: STEM a) HAADF and b) BF images of the sample with $x = 0.35$. c) Atomic resolution STEM HAADF. d) High magnification STEM HAADF of the area close to the substrate. (e-f) Corresponding STEM-EDS maps for In-L_α (red) and Ga-K_α (green). g) Cationic percentage for In-L_α (red) and Ga-K_α (green) across the yellow arrow marked in f). The measured thickness of this sample is 450 nm

sample with $x = 0.22$ shows distinct regions. One with a homogeneous cation distribution and another with a clear contrast indicating cation segregation. This segregation is observed throughout the sample with $x = 0.35$ as shown in Fig. 2.12. The high angle annular darkfield and brightfield images of Fig. 2.12 a) and b) as well as the Energy Dispersive X-Ray Spectroscopy (EDX) false-color image in e) show that In and Ga-rich regions form alternating layers with an angle between 45° and 55° with respect to the substrate. A closer look at the substrate/thin film interface in Fig. 2.12d) shows that a cubic, about 10 nm thick $(In,Ga)_2O_3$ layer forms first, followed by triangular shaped Ga-rich crystals, which seem to initiate the segregation process [2]. The thickness of the Ga-rich (In rich) regions is about 10 to 15 nm (40 nm) as shown in the EDX line scan of Fig. 2.12g). Further studies are demanded to clarify in detail the mechanism causing the observed cation segregation for a potential explotation in periodic arrangements of heterostructures in, e.g., metamaterials.

[1] H. von Wenckstern, M. Kneiß, A. Hassa, P. Storm, D. Splith, M. Grundmann, Phys. Status Solidi B **257**, 1900626 (2020)
[2] S. Montag, D. Splith, M. Kneiß, M. Grundmann, J. Garcia Fernandez, Ø. Prytz, H. von Wenckstern, Phys. Rev. Materials **7**, 094603 (2023)
[3] H. von Wenckstern, Adv. Electron. Mater. **3**, 1600350 (2017).

2.10 Phonon Eigenvector reversal in CuBrI alloy

R. Hildebrandt, C. Sturm, M. Grundmann

Wide-bandgap semiconductors show promising properties regarding higher operation voltages, frequencies and temperatures for devices, while additionally their transparency enables further applications. Many wide-bandgap n-type materials are available nowadays. However, suitable intrinsic p-type materials are still missing. A possible p-type candidate for optoelectronic and thermoelectronic devices is CuI [1]. Tuning its electrical properties can be achieved by alloying with Br, as the dominating Cu vacancy shifts thereby its activation energy [3].

Phononic properties were investigated to gain insight for short range interactions of the CuI-CuBr system. The thin films were deposited by pulsed laser deposition by using an elliptical target made of CuBrI for the alloyed thin films, whereas for the unalloyed films a CuI and a CuBr target was used. Raman measurements in the transparent regime were done with an excitation wavelength of 532 nm to determine the energies of the longitudinal (LO) and transversal (TO) optical phonon. The measured Raman specra are shown in Fig. 2.13a. The Br-content of the samples was determined by using Vegards-law by means of X-ray diffraction (XRD) measurements.

The energy of the TO mode energy as a function of the Br composition is shown in Fig. 2.13b. A bowing of the phonon mode energy is observable. This bowing cannot be explained by the sophisticated modified random element isodisplacement model (MREI) proposed by Chang and Mitra[2]. Considering other optical and vibrational properties of CuBr crystals, the proposed eigenvector reversal (EVR) as proposed by Serrano et al. is followed [4] the observed behaviour of the TO mode energy on the composition can be nicely described. These adjustments require an exchange of the dominant mass *M* with the non-dominant mass *m* for the phonon eigenstates.

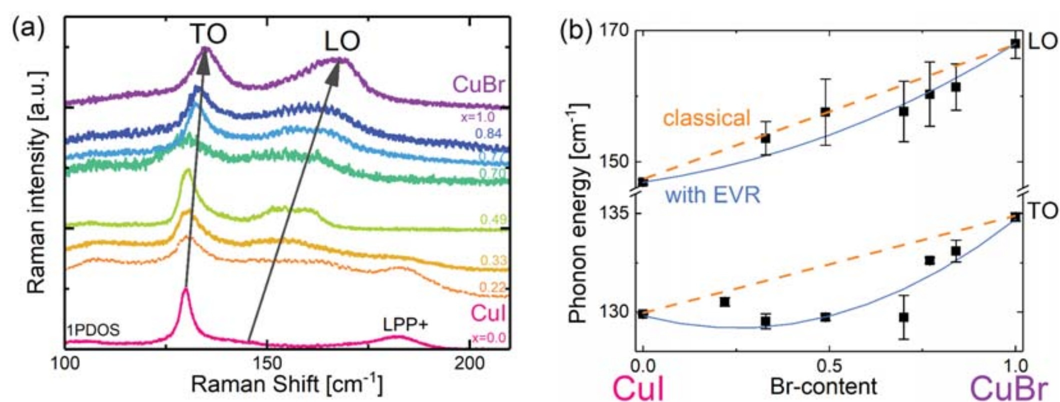

Figure 2.13: (a) Raman spectra of $Cu_{1-x}Br_xI$ thin films for selected Br composition *x*. (b) TO phonon energy as a function of the Br composition *x*. The expected model determined by the MREI model is shown as orange dashed line. The solid blue line represents the calculated mode energy by using the modified MREI model with the EVR.

[1] M. Grundmann *et al.* Phys. Status Solidi A **210**, 9 (2013). doi:10.1002/pssa.201329349
[2] I.F. Chang, S. S. Mitra Phys. Rev. **172**, 3 (1968). doi:10.1103/PhysRev.172.924
[3] N. Yamada *et al.* Adv. Func. Mat. **30**, 34 (2020). doi:10.1002/adfm.202003096
[4] J. Serrano *et al.* Phys. Rev. B **65**, 12 (2002). doi:10.1103/PhysRevB.65.125110

2.11 Two-photon absorption channels in CuI

A. Müller, L. Käferstein, L. Trefflich, S. Blaurock *, H. Krautscheid *, M. Grundmann, C. Sturm

*Universität Leipzig, Institute of Inorganic Chemistry, Johannisallee 29, 04103 Leipzig.

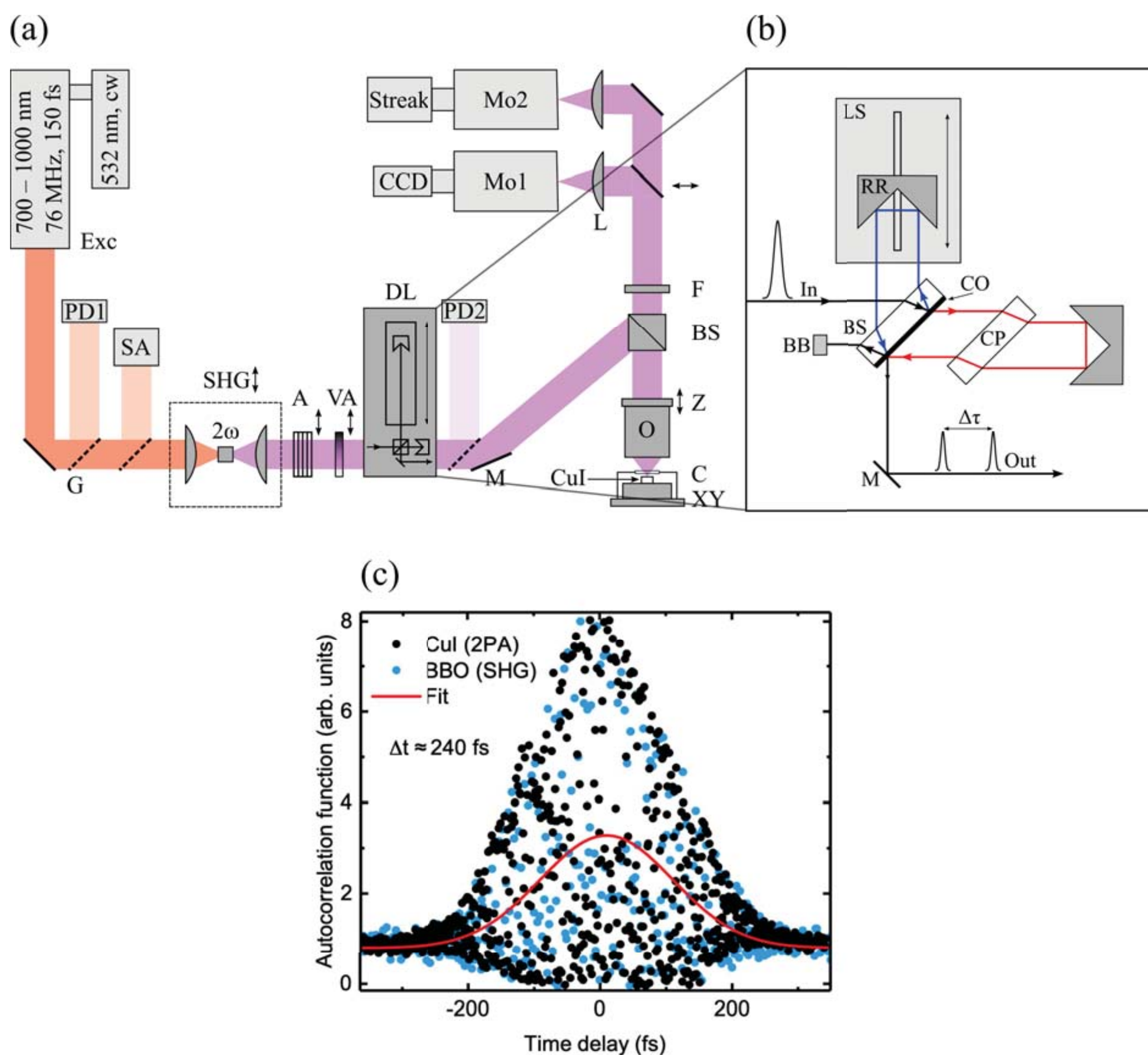

Figure 2.14: (a) - Sketch of the PL setup with Exc - excitation source, G - glass plate, PDX - photodiodes, SA - spectrometer, SHG - rail for second harmonic generation (optional), A and VA - attenuators (optional), DL - delay line, M - mirrors, BS - beamsplitter, Z - piezo stage, O - microscope objective, C - helium flow cryostate, CuI - CuI sample, XY - x-y-linear stages, F - laser filter, L - lenses, MoX - monochromators, CCD - CCD detector, Streak - Streak camera. (b) -Detailed beam path within the delay line with In - incoming laser pulse, BS - beam splitter, CO - beam splitter coating, LS - linear stage, RR - retroreflectors, CP - compensation plate, M - mirror, Out - delayed pulses, BB - beam block. (c) - Measured interferrometric autocorrelation functions of CuI (black symbols) and BBO (blue symbols) with the corresponding fitting curve (red solid line).

CuI is widely recognized as a promising material for various applications in opto-

electronics [1]. Therefore, it is crucial to investigate not only its linear optical properties but also its nonlinear optical properties. We have recently reported that CuI is an efficient multi-photon absorbing material [2] and have also found indications of a defect level at an energy around 2.6 eV. This level can serve as a real intermediate state for a two-step absorption (2SA) process, which must be clearly distinguished from the virtual intermediate level involved in real two-photon absorption (2PA). For virtual level assisted 2PA, the power law $I \propto P^n(E_{exc})$ yields an exponent $n = 2$. However, at this energy we observe a decrease of the exponent n down to ≈ 1.5, which can be attributed to the saturation of a defect's occupancy [3]. Furthermore, Koyasu *et al.* [4] have predicted a defect level at an energy of 2.7 eV using DFT calculations. Lastly, photoluminescence spectra of CuI reveal a broad DAP band extending down to 2.70 eV which may support a 2SA process. To prove that 2SA process occurs in this energy region, we determine the lifetime of the intermediate state using interferometric autocorrelation technique. In the case of a 2PA via a virtual state, the width of the autocorrelation function yields the pulse duration of the laser. However, the function is expected to broaden for longer lifetimes if real states are involved in the 2SA process.

To conduct these measurements, our existing photoluminescence (PL) setup was expanded by a Michelson-type interferometer. The setup is depicted in Fig. 2.14(a) and 2.14(b). From the interferometric autocorrelation function

$$I(\tau) \propto \int_{-\infty}^{\infty} \left|[E(t) + E(t-\tau)]^2\right|^2 \mathrm{d}t, \tag{2.8}$$

the important peak-to-background ratio was deduced to be $I(0) : I(\infty) = 8 : 1$, which validates the accuracy of the measurement process. Room temperature measurements of CuI and a BBO crystal excited with 795 nm are shown in Fig. 2.14(c). In this excitation range no defect is expected. Therefore, the broadening of the autocorrelation function reflects the lasers pulse duration. The peak-to-background ratio of 8 : 1 was achieved, proving the proper alignment of our setup and the curves exhibit the same widths as the laser pulse. This proves a pure 2PA via virtual states and renders CuI suitable as a nonlinear medium for autocorrelation measurements. A room temperature autocorrelation measurement with 440 nm excitation wavelength is shown in Fig. 2.15(a), where no broadening can be observed. Since potential defect levels may not be occupied at room temperature, the measurements were repeated at low temperatures (10 K). Fig. 2.15(b)-2.15(d) show the measurements for (440, 460, 480) nm excitation wavelengths.

Indeed, the measured functions look significantly different in terms of line shape and broadening compared to those performed at room temperature. The broadening increases from 170 fs up to 270 fs for an excitation wavelength of 440 nm and 460 nm, respectively. Furthermore, a wing-like structures appear on the tails. Hattori *et al.* [5] also measured such structures and determined a modified autocorrelation function through Bloch equation analysis, incorporating the lifetime T of the real intermediate state. The autocorrelation function is then given by [5]:

$$I(\tau) \propto \int_{-\infty}^{\infty} \mathrm{d}t \int_{-\infty}^{t} \mathrm{d}t' \, [E(t) + E(t-\tau)]^2 \, [E(t') + E(t'-\tau)]^2 \, \mathrm{e}^{-(t-t')/T}. \tag{2.9}$$

[1] M. Grundmann, et al.: Phys. Status Solidi A **210**, 1671 (2013), doi:10.1002/pssa.201329349

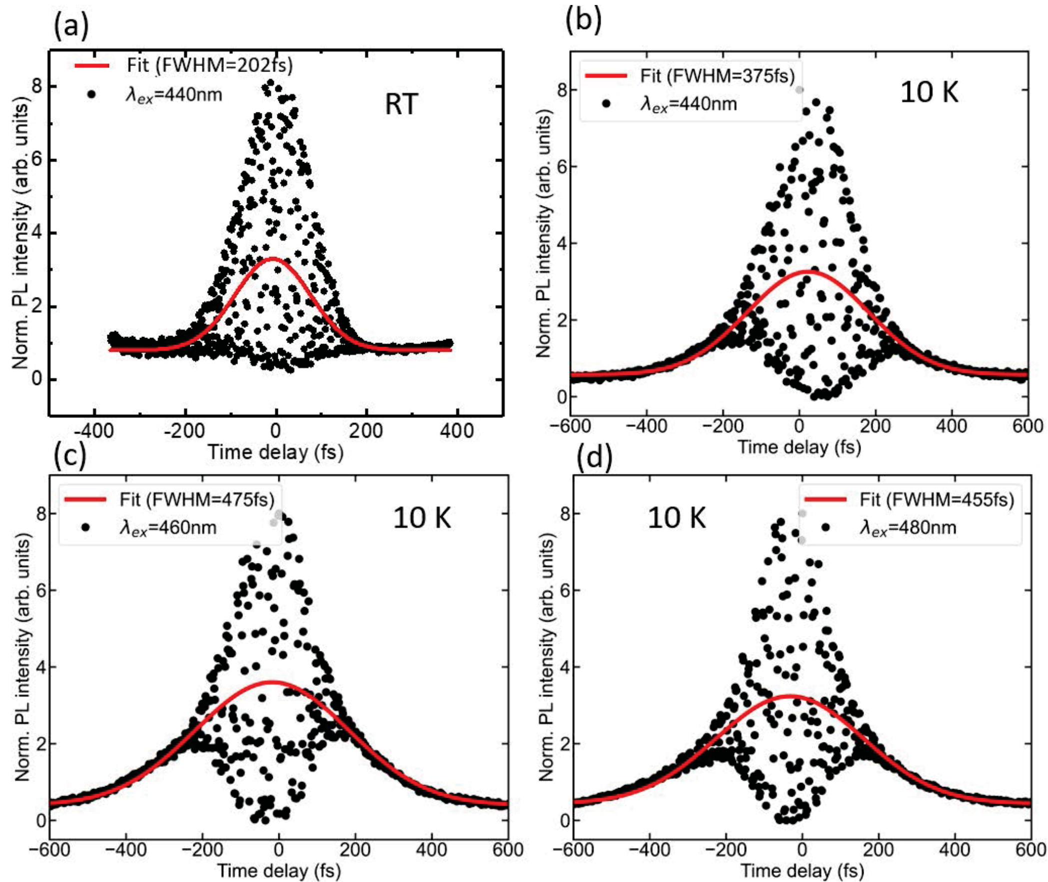

Figure 2.15: Measured interferometric autocorrelation functions (black symbols) with corresponding fit curves (red solid lines) for different excitation wavelengths and temperatures. (a) - 440 nm excitation wavelength at room temperature, (b-d) - (440, 460, 480) nm excitation wavelength at 10 K.

[2] A. Müller, et al.: Appl. Phys. Lett. **123**, 122103 (2023), doi:10.1063/5.0167096
[3] S. L. Chen, et al.: Appl. Phys. B **108**, 919 (2012),Â doi:10.1007/s00340-012-5138-y
[4] S. Koyasu, et al.: J. Appl. Phys. **125**, 115101 (2019), doi:10.1063/1.5082865
[5] T. Hattori, et al.: Jpn. J. Appl. Phys. **39**, 4793 (2000), doi:10.1143/JJAP.39.4793

2.12 Emission from propagating Bloch surface wave polaritons

S. Henn, A. Müller, C. Sturm, M. Grundmann

Light travelling inside a material comprises a mixture of an electromagnetic wave as well as a polarization wave, that can exchange quantized energy ($\hbar\omega$) with other systems, e.g. the vacuum radiation field, and these energy quanta are called polaritons [1]. Prominent examples of these are exciton-polaritons, where the photon interacts with the electron-hole pairs of a semiconductor, e.g. inside a microcavity [2], displaying a wide variety of interesting physical phenomena, like low-threshold lasing and Bose-Einstein condensation [3].

Another platform for the formation of exciton-polaritons is a distributed Bragg reflector (DBR) with a truncated surface layer. This surface layer supports an evanescent wave propagating along the interface, the so-called Bloch surface wave (BSW) [4]. Its dispersion lies outside the vacuum light cone and cannot couple to the ambient electromagnetic field, which leads to a large inherent lifetime but requires a coupling mechanism [5].

By depositing a semiconducting ZnO surface layer on the reflector and using a prism coupler, these modes can be strongly coupled to excitons and form Bloch surface wave polaritons (BSWP). These are stable up to 430 K [6], due to the large exciton binding energy of 60 meV in ZnO. This holds several advantages compared to exciton-polaritons in conventional planar microcavities: a reduced complexity of production, due to the less required number layers, and direct access to the mode-supporting layer for the deposition of further structures, e.g. interferometers, gratings, which is useful for application purposes. Additionally, the Bloch-polariton has no ground state, i.e. $k \neq 0$ and inherits the low-loss-nature of BSW, promising large propagation lengths.

Though prism couplers are sufficient for the observation of BSWP in the far field, it is very hard to gain information on the position of excitation or the lateral decay of the BSWP as the light is coupled into the structure through the substrate side, i.e. 'the backside'. In order to obtain a better spatial control of the excitation/ detection of BSWP it is possible to use optical diffraction gratings with lattice constants at a sub-micron scale, positioned directly in the mode-supporting surface layer. Covering an area of around $50 \times 50\,\mu m^2$ such gratings approximately shift the BSW dispersion by $\Delta k_{\|} \sim 2\pi m/L$, where L and m denote the lattice constant of the grating and the diffraction order, respectively.

In order to obtain high quality ZnO, the substrate temperature was held at 650 °C which in turn leads to a high roughness in our pulsed-laser deposition grown samples that is on the order of the depth of the gratings. To circumvent this, Dr. Dornberg from the Leibniz institute for surface engineering applied an ion-beam assisted smoothing process for the ZnO layers and we investigated the structural and optical consequences of this treatment [7]. Though the smoothness of the surface layer was reduced by roughly 70 %, allowing for the fabrication of gratings, the emission from exciton transitions is reduced (cf. Fig.2.16(a)-(d)).

Nonetheless, it was possible to detect strongly-coupled BSW and excitons in the smoothed samples. In Fig. 2.16(g) the emission from the lower polariton branch (LPB) obtained from non-resonant excitation is shown for different lattice constants, L, of the gratings. For $L = 500$ nm the wavevector shift is too small for the LPB to fall within our finite numerical aperture, NA= 0.4. For $L = 400$ nm and $L = 300$ nm the polaritons for $k_{\|} < 0$ ($k_{\|} > 0$) are obtained for angles of incidence $\theta < 0^\circ$ ($\theta > 0^\circ$) and $\theta > 0^\circ$ ($\theta < 0^\circ$), respectively.

If the excitation region is separated incrementally by d from the grating detection area, the intensity of the polariton emission, which is proportional to the number of polaritons, can be tracked as a function of d, i.e. $I(d)$. This allows to extract the propagation length from an exponential decay model $\propto \exp(-ix/D)$, while taking into account decreasing intensity resulting from a radially homogeneous distribution of propagation directions. As a result (cf. Fig. 2.16(f)), we obtained propagation lengths on the order of $(1-10)\,\mu$m that are larger than the inverse absorption coefficient in pristine ZnO, which usually governs the length scale of electromagnetic intensity decay.

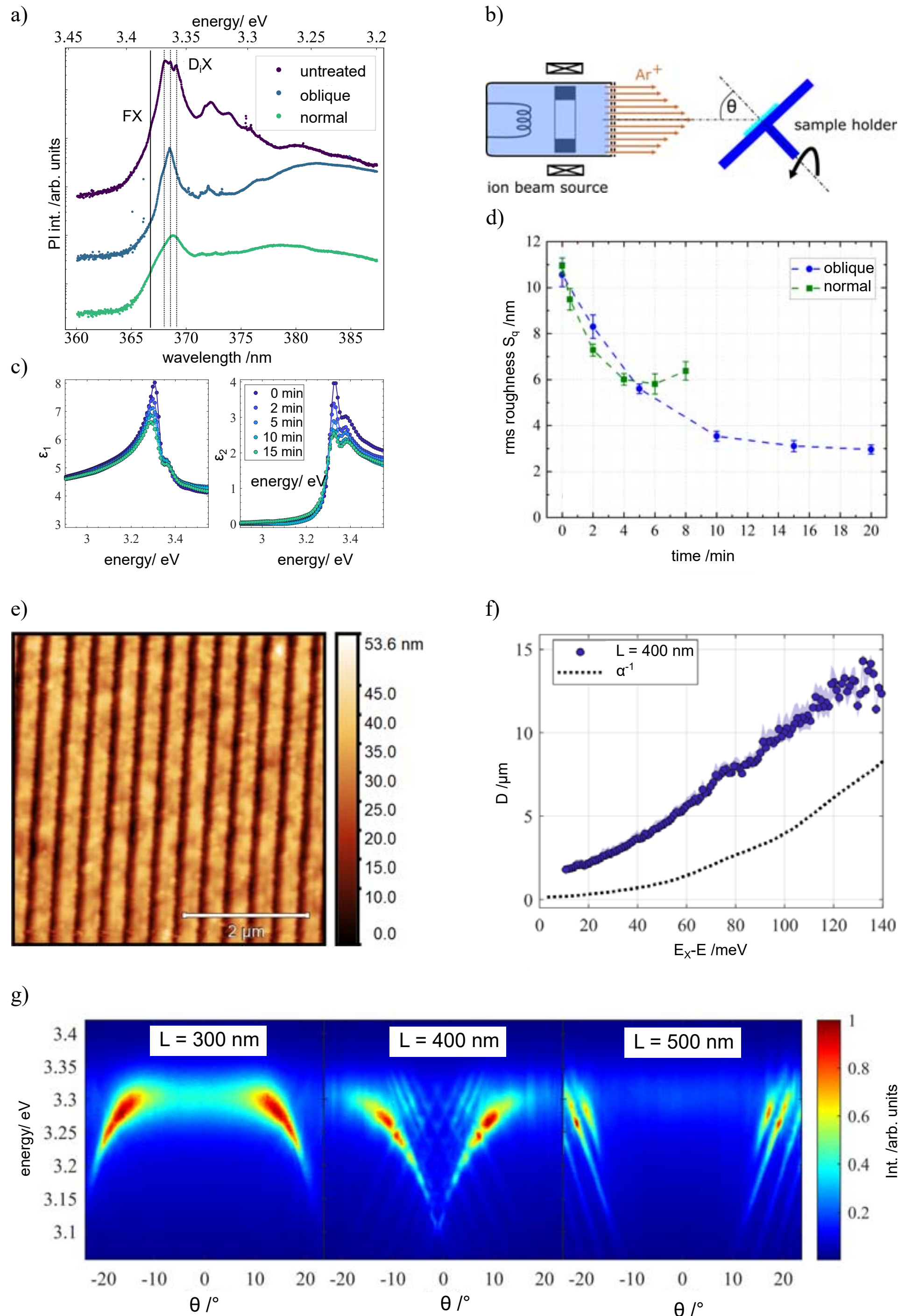

Figure 2.16: a) Photoluminescence spectra at 10 K of the pristine and smoothed samples at different angles of incidence, b) schematic of the smoothing process, c) dielectric function of ZnO in between smoothing steps for oblique angle of incidence, d) ZnO roughness as a function of smoothing time, e) AFM scan of the gratings on the smoothed sample, L= 400 nm, f) propagation length *D* extracted from the model, g) PL images of polariton branches for different grating geometries.

We assume that this is due to the small overlap of the field profile of the bare BSW mode with the active layer. These findings open the path to investigating interacting

propagating Bloch surface wave polaritons.

[1] C. Klingshirn: Semiconductor Optics 4th Ed. (Springer-Verlag, Berlin Heidelberg, 2012) doi:10.1007/978-3-642-28362-8
[2] R. Schmidt-Grund *et al.*, Appl. Phys. B **93**, 331-337 (2008). doi:10.1007/s00340-008-3160-x
[3] J. Klaers *et al.*, Nature **468**, 545-548 (2010) doi:10.1038/nature09567
[4] P. Yeh *et al.*, Appl. Phys. Lett. **32**, 104 (1978); doi:10.1063/1.89953
[5] H. Raether: Surface Plasmons on Smooth and Rough Surfaces and on Gratings 1st Ed. (Springer-Verlag Berlin Heidelberg, 1988) doi:10.1007/BFb0048317
[6] S. Henn *et al.*, New J. Phys. **23**, 09031 (2021) doi:10.1088/1367-2630/ac2452
[7] S. Henn *et al.*, Thin Solid Films **794**, 140290 (2024) doi:10.1016/j.tsf.2024.140290

2.13 Optimization of vertically graded $Mg_xZn_{1-x}O$ layers for the use in wavemeters

C. Brunhuber, L. Trefflich, D. Splith, C. Sturm, M. Grundmann

In [1] a new concept for a forward-looking, monolithic and ultra-compact wavemeter was proposed, that is able to determine the wavelength of monochromatic radiation in a broad spectral range. It is based on two photodetectors stacked on each other. Incoming light first hits an absorption layer with a vertically graded alloy composition. The proportion of the light that is absorbed depends on its wavelength. The remaining light is absorbed in a homogeneous absorber. The ratio of the generated photocurrents relates to the wavelength of the incident radiation. In this work we compared four different designs for the graded layer and realized such wavemeter devices using a $Mg_xZn_{1-x}O$ alloy system. Within the graded absorption layer the Mg-content increases from $x = 0$ to $x \approx 0.4$, so that for all compositions the wurtzite structure is obtained. The two absorbers were deposited on opposite sides of an a-sapphire substrate by pulsed laser deposition, using a vertical continuous composition spread (VCCS-PLD) technique to obtain the graded layer.

Before we fabricated the wavemeter, four different designs of the vertically graded were investigated in order to find best suited one for a wavemeter device. i) and ii) In design A_1 and A_2, the composition x increases in growing direction, i.e., the layer with the lowest Mg concentration, and thus with the smallest band gap energy, is at the substrate. The design A_1 consists of seven single layers, which were all grown with the same number of laser pulses, while in A_1 a slightly thicker bottom and top layer was chosen. iii) In design B a inverted gradient compared to design A was realized, i.e., starting with the Mg-richest layer and ends up with ZnO. iv) In design C the same as structure as in design A_1 was used, except that an additional ZnO layer was deposited on top of the structure. The XRD $2\theta - \omega$-scans shown in Fig. 2.17(a) indicate no phase separation in all deposited gradients and the wurtzite structure was confirmed for all films. The c-plane ZnO peaks are shifted to higher angles due to the incorporation of Mg. Fig. 2.17(b) shows the spectrally resolved photocurrent for photon energies from 2.75 eV to 5.00 eV. Due to the high signal intensity and an almost constant photocurrent above

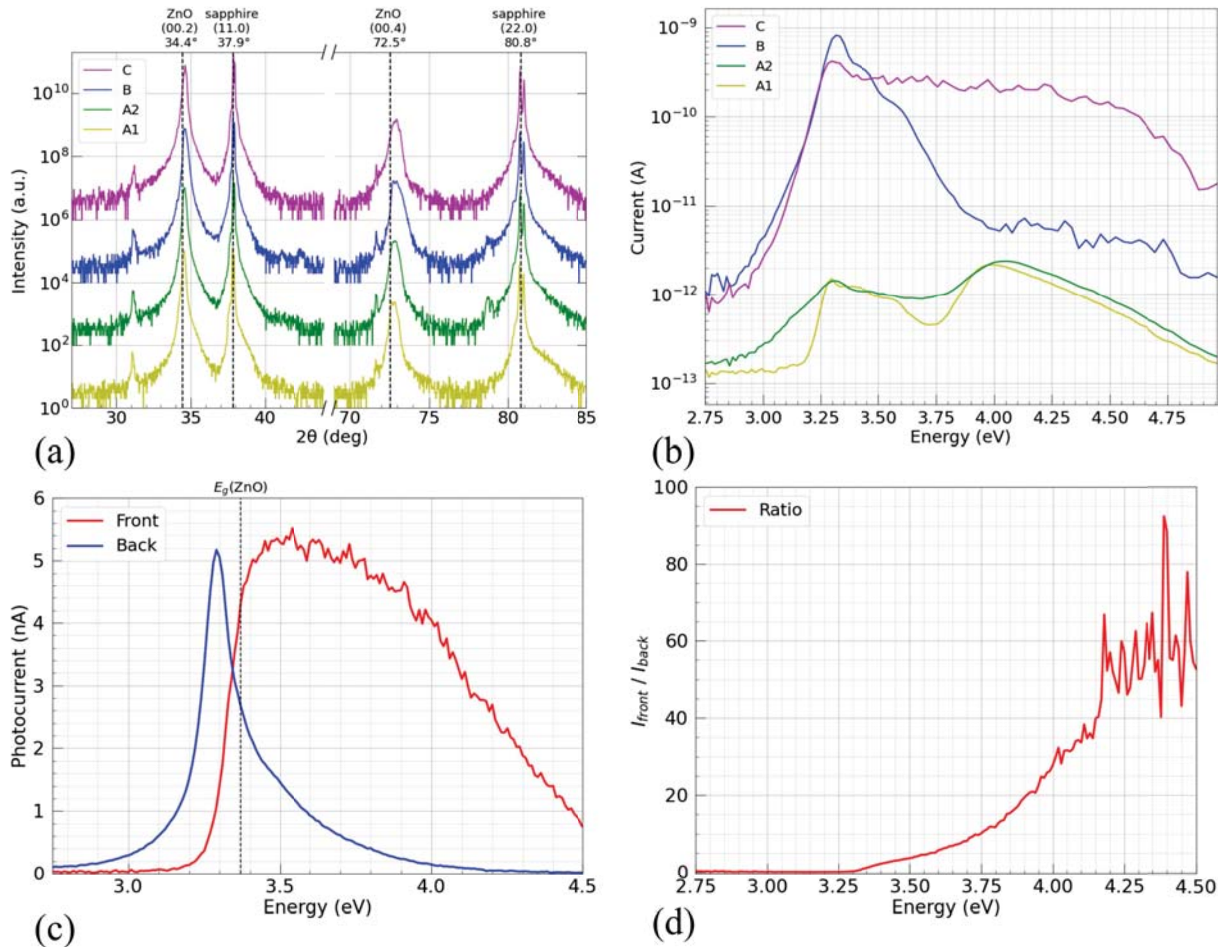

Figure 2.17: (a)XRD 2θ-ω-scans of the four different gradient designs. The peaks of the a-plane oriented sapphire substrate and c-plane wurtzite ZnO are marked by black dashed lines. (b) Spectrally resolved photocurrents generated in the gradients. (c) Photocurrents measured in the graded front layer (red) and the homogeneous back layer (blue) of a wavemeter device. (d) The ratio I_{front}/I_{back} of the currents in (c) for photon energies from 2.75 eV to 4.5 eV.

3.3 eV, while the intensity of the light coming from a Xe-lamp decreases exponentially, design C is the most promising design for the wavemeter.

A wavemeter device was built with a homogeneous ZnO layer on the back side and a vertically graded $Mg_xZn_{1-x}O$, using design C, on the front side of an a-plane oriented sapphire substrate. Fig. 2.17(c) shows the photocurrents generated in the two layers when light enters the wavemeter from the front contact. The current in the graded layer (red) strongly increases when the photon energy overcomes the band gap energy of ZnO and stays on a high level of about 5 nA up to 3.9 eV. For larger energies the photocurrent decreases almost linear with increasing photon energy. The current on the back side has its maximum below the ZnO bandgap energy and drops exponentially with increasing energy. This decrease can be attributed to the strong absorption of the light in the gradient layer in front of the substrate, which reduces the number photons reaching the back contact. The ratio of the two photocurrents (I_{front}/I_{back}) is shown in Fig. 2.17(d). The ratio is almost monotonous increasing in the region from 3.3 eV to 4.0 eV and looks similar to the ratio predicted in [1]. For higher energies strong noise is received, because of the low currents measured in both layers.

[1] M. Grundmann: Phys. Stat. Sol. A **215**, 1800651 (2018)

2.14 Exceptional points in optically anisotropic materials

C. Sturm, M. Grundmann

In materials, having a lower crystal symmetry than the cubic one, the two eigenmodes differ in general from each other with respect to their polarization state (eigenstate) and propagation properties, i.e. refractive index (eigenvalue), which causes among other things birefringence. In the transparent spectral range, it is well known, that the propagation properties can degenerate. For materials, which crystalizes in a hexagonal, tetragonal or trigonal crystal structure, there exists two direction where the propagation properties degenerate. As these two directions point in opposite directions, they form an axis, and thus materials with these crystal structure are called optically uniaxial. For materials which crystallizes in an orthorhombic, monoclinic or triclinic crystal structure, two axis exist, where the propagation properties degenerate, and they are called optically biaxial. [1]

An interesting situation appears in the absorbing spectral range where only one eigenmode exists. This means, in contrast to the transparent spectral range, the propagation properties and the polarization state degenerate. This was firstly pointed out by W. Voigt in 1902 for orthorhombic crystals [2] and takes also place in monoclinic and orthorhombic crystals [3]. The corresponding eigenmode is either right or left circular polarized. This degeneration can also be considered as an exceptional point (EP) in the energy-momentum space. The EPs appear pair-wise in bulk materials and two of them forming an axis, called singular optic axis. Four of such singular optic axes can exists in bulk materials. We developed an analytical expression for the spatial distribution of these axes. [4] By means of this expression we could demonstrate that the spatial distribution of these axes are connected with each other, even for triclinic materials.

The presence of these EPs is not limited to optically biaxial materials. If the phase front and the amplitude front are not coplanar to each other, like it happens if interfaces are involved, EPs can appear in optically uniaxial materials. [5] It should be noted, that in this case, two directions do not necessarily point in opposite directions and thus, singular optic axes are not necessarily formed.

Due to the degenerate eigenstate, an arbitrarily polarized waved cannot be described by a linear combination. As a result, the reflection and transmission of a wave at an interface cannot be determined, if an EP is involved. We developed two formalism in order to the propagation of the arbitrarily polarized wave at an EP [5]: i) In contrast to the classical used approach, one have to take into account the spatial dependence of the field amplitude or ii) the change of the electric field is described by a propagation matrix. For a wave, with a different polarization than the eigenstate of the EP, a non-exponential decay is obtained. Furthermore, it is shown, that the polarization of the wave changes along its propagation to those of the eigenstate. By means of the two formalism, the reflection and transmission properties at an interface can be calculated, even in the case EPs are involved.

[1] M. Born and E. Wolf: *Principles of Optics: Electromagnetic Theory of Propagation, Interference and Diffraction of Light, 7th ed.* (Cambridge University Press, 1999).

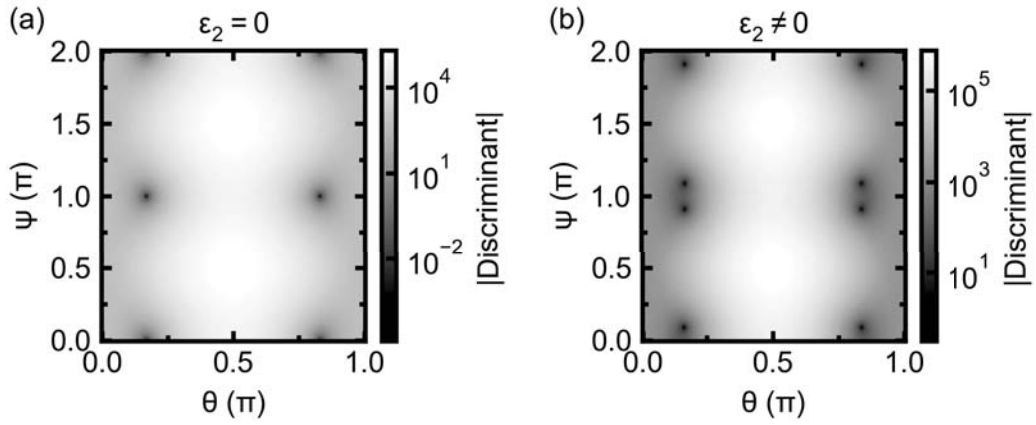

Figure 2.18: The discriminant of the wave equation for a propagating wave in ZnO for (a) the transparent spectral range at $E = 2.5\,\mathrm{eV}$ and (b) absorption spectral range at $E = 4.0\,\mathrm{eV}$. The waves are propagating in the in the x-z plane and with a wave vector component $k_x = 2\pi\sin(4\pi/9)/\lambda$. The angels ψ and θ represents the rotation of the crystal around the z and x-axis, respectively. The crystallographic c-axis coincide with the z-axis for $(\psi, \theta) = (0, 0)$.

[2] W. Voigt: Ann. Phys. **314**, 367 (1902), doi:10.1002/andp.19023141006
[3] M. V. Berry and M. R. Dennis: Proc. R. Soc. London, Ser. A **459**, 1261 (2003)., doi:10.1098/rspa.2003.1155
[4] M. Grundmann and C. Sturm: Phys. Rev. A **103**, 053510 (2021), doi:10.1103/PhysRevA.103.053510
[5] C. Sturm: Adv. Photonics Res. 2300235 (2024), doi:10.1002/adpr.202300235

3

Funding, Organizational Duties, External Cooperations

3.1 Funding

Raman-Streuung in anisotropen Kristallen
Prof. Dr. M. Grundmann
DFG GR 1011/33-2

Raman-Streuung in anisotropen Kristallen
Dr. C. Sturm
DFG STU 647/5-2

Bauelemente mit vertikalem Kompositionsgradient
Prof. Dr. M. Grundmann
DFG GR 1011/42-1

Zwischenband-Solarzellen auf Basis Übergangsmetall-substitutierter Indium-thiospinelle
PD Dr. H. von Wenckstern
DFG WE 4620/3-1

Remanentes Schalten von Bloch-Polaritonen
Dr. C. Sturm
DFG STU 647/2-1

Sn(II)-Verbindungen als transparente, leitfähige Oxid-Halbleiter vom p-Typ
Prof. Dr. M. Grundmann
DFG GR 1011/44-1

"High entropy" Halbleiter-Legierungen
Prof. Dr. M. Grundmann
DFG GR 1011/46-1

"High entropy" Halbleiter-Legierungen
PD Dr. H. von Wenckstern
DFG WE 4620/8-1

Koordinationsfonds
Prof. Dr. M. Grundmann
DFG GR 1011/41-2 within FOR 2857 *Kuperiodid als multifunktionaler Halbleiter*

Mikrostruktur-basierte Optimierung von CuI-Dünnfilmen mittels Laser-Plasmaabscheidung
Prof. Dr. M. Lorenz
DFG LO 790/7-2, P01 within FOR 2857 *Kupferiodid als multifunktionaler Halbleiter*

Sputter-Abscheidung amorpher und kristalliner Kupfe-riodid-Dünnfilme und Kupferiodid-basierter Legierungshalbleiter
Dr. S. Vogt
DFG VO 2777/1-1, P03 within FOR 2857 *Kupferiodid als multifunktionaler Halbleiter*

Elektrische Eigenschaften von CuI Dünnfilmen und Volumenkristallen und Herstellung von CuI-basierten Bauelementen
PD Dr. H. von Wenckstern
DFG WE 4620/5-2, P05 within FOR 2857 *Kupferiodid als multifunktionaler Halbleiter*

Optische Eigenschaften von Kupferiodid, dotierten Kupferiodid und Kupferiodid basierten Legierungshalbleitern
Dr. C. Sturm
DFG STU 647/3-2, P06 within FOR 2857 *Kupferiodid als multifunktionaler Halbleiter*

Ultrakompaktes Spektrometer – UltraSPEC2
Prof. Dr. M. Grundmann
VIP+, BMBF 03VP08180

Growth and fundamentals of oxides for electronic applications – GraFOx II
Prof. Dr. M. Grundmann, PD Dr. H. von Wenckstern
Leibniz Gemeinschaft W40/2019

Wettbewerbsfähiger Deutscher Quantenrechner: TP Herstellung von Diamantproben mit gekoppelten NV Zentren, Aufbringen von leiterbahnen zur Mikro- und Radiowellenankopplung – CoGeQ
Prof. Dr. M. Grundmann, Prof. Dr. J.B. Meijer
BMBF 13N16097

3.2 Organizational Duties

M. Grundmann

- Dean of the Faculty of Physics and Earth System Sciences
- Sprecher der Forschungsgruppe FOR 2857 "Copper Iodide as Multifunctional Semiconductor", https://research.uni-leipzig.de/for2857/
- Sprecher der Fächerübergreifenden Arbeitsgemeinschaft Halbleiterforschung Leipzig (FAHL), https://home.uni-leipzig.de/fahl/
- Sprecher des Freundeskreis der Fakultät für Physik und Geowissenschaften
- Member Editorial Board: Physica Status Solidi (a), (b), RRL, MDPI nanomaterials, Phys. Rev. Research

- Member International Advisory Board: Advanced Electronic Materials
- Project Reviewer: diverse
- Referee: Applied Physics Letters, Electronics Letters, Journal of Applied Physics, Nature, Physica E, Physical Review B, Physical Review Letters, Physica Status Solidi, Advanced Materials, u.a.

M. Lorenz

- Member Editorial Board: Journal of Physics D: Applied Physics (IOP, Bristol, U.K.), Journal Materials (MDPI, Basel, Switzerland)
- Project Reviewer: Deutsche Forschungsgemeinschaft, Alexander von Humboldt - Stiftung
- Referee: ACS Applied Nano Materials, Advanced Materials, Advanced Electronic Materials, Applied Physics Letters (APL), coatings (MDPI), Dalton Transactions, fibers (MDPI), Journal of Crystal Growth, Journal of Physics D: Applied Physics, Journal of Alloys and Compounds (JALCOM), Journal of Applied Physics (JAP), Journal of Magnetism and Magnetic Materials (JMMM), materials (MDPI), nanomaterials (MDPI), small (Wiley VCH), Thin Solid Films

D. Splith

- Referee: Applied Physics Express, Physica Status Solidi A, IEEE Transactions on Electron Devices

C. Sturm

- Referee: ACS Nano, Appl. phys. Lett., Applied Optics, Alexander von Humboldt Stiftung, Journal of applied Physics, J. Phys. Chem. Lett., Phys. Rev. B, Phys. Status Solidi RRL, Sci. Rep.

H. von Wenckstern

- Project Reviewer: Deutsche Forschungsgemeinschaft, National Science Centre Poland
- Associate Editor: Journal of Electronic Materials
- Referee: ACS Materials and Interfaces, Advanced Functional Materials, Annalen der Physik, Applied Physical Letters, APL Materials, Electronic Device Letters, Journal of Applied Physics, Material Science in Semiconductor Processing, Physica Status Solidi, Scientific Reports, Solid State Electronics, Superlattices and Microstructures, Thin Solid Films, u.a.

3.3 External Cooperations

Academic

- Leibniz-Institut für Oberflächenmodifizierung e. V., Leipzig, Germany
  Prof. Dr. A. Anders, Prof. Dr. S. Mayr, Dr. C. Bundesmann, Dr. A. Lotnyk
- Universität Leipzig, Fakultät für Chemie und Mineralogie, Germany
  Prof. Dr. H. Krautscheid, Prof. Dr. R. Denecke, Prof. Dr. O. Oeckler, Dr. V. Gottschalch, Dr. S. Blaurock

- Universität Halle-Wittenberg, Germany
  Prof. Dr. I. Mertig, Prof. Dr. R. Scheer
- Fraunhofer-Institut für Mikrostruktur von Werkstoffen und Systemen IMWS, Halle (Saale), Germany
  Prof. Dr. T. Höche, Dr. C. Patzig, Dr. S. Selle
- Forschungszentrum Dresden-Rossendorf, Germany
  Dr. S. Zhou
- Humboldt-Universität zu Berlin, Germany
  Prof. Dr. N. Koch
- Leibniz-Institut für Festkörperelektronik – Paul Drude (PDI), Berlin, Germany
  Dr. O. Bierwagen
- Universität Magdeburg, Germany
  Prof. Dr. A. Dadgar, Dr. J. Bläsing
- Universität Jena, Germany
  Prof. Dr. C. Ronning, Prof. Dr. S. Botti
- Technische Universität Ilmenau, Germany
  Prof. Dr. S. Krischok, Dr. R. Schmidt-Grund
- Johannes Gutenberg-Universität Mainz, Department Chemie, Germany
  Prof. Dr. S.R. Waldvogel
- Hochschule Mittweida, Laserinstitut, Germany
  Prof. Dr. A. Horn, T. Pflug, M. Olbrich
- University of Canterbury, Christchurch, New Zealand
  Prof. Dr. M. Allen
- Centre de Recherche sur l'Hétéro-Epitaxie et ses Applications (CNRS-CRHEA), Valbonne, France
  Dr. J. Zúñiga-Pérez, Dr. Guy Feuillet
- Western Michigan University, USA
  Prof. Dr. S. M. Durbin
- The Ohio State University, USA
  Prof. Dr. L. Brillson
- Arizona State University, USA
  Prof. F. Ren
- University of Florida, USA
  Prof. S. Pearton
- Katholieke Universiteit Leuven, Belgium
  Dr. V. Lazenka, Prof. Dr. K. Temst
- University of Oslo, Norway
  Prof. Dr. L. Vines
- ELI Beamlines - International Laser Research Centre, Dolní Brežany, Czech Republic
  Prof. J. Andreasson, Dr. S. Richter, Dr. S. Espinoza, Dr. M. Rebarz

Industry

- Freiberger Compound Materials GmbH, Freiberg, Germany
  Dr. G. Leibiger
- First Sensor AG, Berlin, Germany
  Dr. M. Schillgalies
- Optics Balzers Jena GmbH, Jena, Germany
  Dr. A. Rahm
- SaxonQ GmbH, Leipzig, Germany

4

Publications

Journals

J. Borgersen, R. Karsthof, V. Rønning, L. Vines, H. von Wenckstern, M. Grundmann, A.Y. Kuznetsov, K.M. Johansen: *Origin of enhanced conductivity in low dose ion irradiated oxides*, AIP Adv. **13**(1), 015211:1-5 (2023)
doi:10.1063/5.0134699

F. Geng, L. Wang, T. Stralka, D. Splith, S. Ruan, J. Yang, L. Yang, G. Gao, L. Xu, M. Lorenz, M. Grundmann, J. Zhu, C. Yang: *(111)-oriented growth and acceptor doping of transparent conductive CuI:S thin films by spin coating and RF-sputtering*, Adv. Engin. Mater. **25**(11), 2201666:1-5 (2023)
doi:10.1002/adem.202201666

F. Geng, Y.-Ni. Wu, D. Splith, L. Wang, X. Kang, S. Liang, L. Yang, M. Lorenz, M. Grundmann, J. Zhu, C. Yang: *Amorphous Transparent Cu(S,I) Thin Films with Very High Hole Conductivity*, J. Phys. Chem. Lett. **14**(26), 6163-6169 (2023)
doi:10.1021/acs.jpclett.3c01072

M. Grundmann: *Space Charge Region Beyond the Abrupt Approximation*, Phys. Status Solidi B **260**(11), 2300257:1-4 (2023)
doi:10.1002/pssb.202300257

R. Hildebrandt, M. Seifert, J. George, S. Blaurock, S. Botti, H. Krautscheid, M. Grundmann, C. Sturm: *Determination of acoustic phonon anharmonicities via second-order Raman scattering in CuI*, New J. Phys. **25**(12), 123022:1-11 (2023)
doi:10.1088/1367-2630/ad1141

S. Köpp, C. Petersen, D. Splith, M. Grundmann, H. von Wenckstern: *Properties of Schottky barrier diodes on heteroeptixial α-Ga_2O_3 thin flms*, J. Vac. Sci. Technol. A **41**(4), 043411:1-9 (2023) (Editor’s Pick)
doi:10.1116/6.0002651

E. Krüger, V. Gottschalch, G. Benndorf, R. Hildebrandt, A.L. Pereira Brenes, S. Blaurock, M. Bar, S. Merker, C. Sturm, M. Grundmann, H. Krautscheid: *Epitaxial growth of $Ag_xCu_{1-x}I$ on Al_2O_3(0001)*, Phys. Status Solidi B **260**(2), 2200493:1-8 (2023)
doi:10.1002/pssb.202200493

E. Krüger, M. Seifert, V. Gottschalch, H. Krautscheid, C.S. Schnohr, S. Botti, M. Grundmann, C. Sturm: *Optical properties of $Ag_xCu_{1-x}I$ alloy thin films*, AIP Adv. **13**(3), 035117:1-11 (2023)
doi:10.1063/5.0137091

A. Langørgen, Y.K. Frodason, R. Karsthof, H. von Wenckstern, I.J.T. Jensen, L. Vines, M. Grundmann: *Defect level in κ-Ga_2O_3 revealed by thermal admittance spectroscopy*, J. Appl. Phys. **134**(1), 015701:1-6 (2023)
doi:10.1063/5.0150994

M. Lorenz, H. Hochmuth, H. von Wenckstern, M. Grundmann: *Flexible hardware concept of pulsed laser deposition for large areas and combinatorial composition spreads*, Rev. Sci. Instrum. **94**(8), 083905:1-12 (2023)
doi:10.1063/5.0142085

M. Lorenz, P. Storm, S. Gierth, S. Selle, H. von Wenckstern, M. Grundmann: *Diffundierter Sauerstoff als dominierender flacher Akzeptor in p-Typ Kupferiodid-Dünnfilmen*, Chemie Ingenieur Technik **95**(11), 1786-1793 (2023)
doi:10.1002/cite.202300007

S. Luo, L. Trefflich, S. Selle, R. Hildebrandt, E. Krüger, S. Lange, J. Yu, C. Sturm, M. Lorenz, H von Wenckstern, C. Hagendorf, T. Höche, M. Grundmann: *Ultrawide Bandgap Willemite-Type Zn_2GeO_4 Epitaxial Thin Films*, Appl. Phys. Lett. **122**(3), 031601:1-7 (2023)
doi:10.1063/5.0130946

S. Montag, D. Splith, M. Kneiß, M. Grundmann, J. Garcia Fernandez, Ø. Prytz, H. von Wenckstern: *Cation segregation observed in an $(In,Ga)_2O_3$ material thin film library beyond the miscibility limit of the bixbyite structure*, Phys. Rev. Mater. **7**(9), 094603:1-9 (2023)
doi:10.1103/PhysRevMaterials.7.094603

A. Müller, S. Henn, E. Krüger, S. Blaurock, H. Krautscheid, M. Grundmann, C. Sturm: *Two- and three-photon absorption in bulk CuI*, Appl. Phys. Lett. **123**(12), 122103:1-5 (2023)
doi:10.1063/5.0167096

C. Petersen, S. Vogt, M. Kneiß, H. von Wenckstern, M. Grundmann: *PLD of α-Ga_2O_3 on m-plane Al_2O_3: Growth regime, growth process, and structural properties*, APL Mater. **11**(6), 061122:1-8 (2023)
doi:10.1063/5.0149797

F. Schöppach, D. Splith, H. von Wenckstern, M. Grundmann: *Oxygen Plasma Treatment to Enable Indium Oxide MESFET Devices*, Adv. Electron. Mater. **9**(11), 2300291:1-7 (2023)
doi:10.1002/aelm.202300291

T. Schultz, M. Kneiß, P. Storm, D. Splith, H. von Wenckstern, C.T. Koch, A. Hammud, M. Grundmann, N. Koch: *Growth of κ-$([Al,In]_xGa_{(1-x)})_2O_3$ Quantum Wells and their Potential for Quantum Well Infrared Photodetectors*, ACS Appl. Mater. Interfaces **15**(24), 29535-29541 (2023)
doi:10.1021/acsami.3c02695

A. Sharma, O.T. Ciubotariu, P. Matthes, S. Okano, V. Zviagin, J. Kalbácová, S. Gemming, C. Himcinschi, M. Grundmann, D.R.T. Zahn, M. Albrecht, G. Salvan: *Optical and magneto-optical properties of pulsed laser-deposited thulium iron garnet thin films*, Appl. Res. **3**(2), e202200064:1-11 (2023)
doi:10.1002/appl.202200064

T. Stralka, M. Bar, F. Schöppach, S. Selle, C. Yang, H. von Wenckstern, M. Grundmann: *Grain and grain boundary conduction channels in copper iodide thin flms*, Phys. Status Solidi A **220**(6), 2200883:1-8 (2023)
doi:10.1002/pssa.202200883

L. Thyen, D. Splith, M. Kneiß, M. Grundmann, H. von Wenckstern: *Masked-assisted radial-segmented target pulsed-laser deposition: A Novel Method for Area-Selective Deposition using Pulsed-Laser Deposition*, J. Vac. Sci. Technol. A **41**(2), 020801:1-5 (2023) (Editor's Pick)
doi:10.1116/6.0002275

S. Vogt, C. Petersen, M. Kneiß, D. Splith, T. Schultz, H. von Wenckstern, N. Koch, M. Grundmann: *Realization of conductive n-type doped* α*-*Ga_2O_3 *on m-plane sapphire grown by a two step pulsed laser*, Phys. Status Solidi A **220**(3), 2200721:1-6 (2023)
doi:10.1002/pssa.202200721

E.M. Zollner, S. Selle, C. Yang, K. Ritter, S. Eckner, E. Welter, M. Grundmann, C.S. Schnohr: *Oxygen-induced phase separation in sputtered Cu-Sn-I-O thin films*, Phys. Status Solidi A **220**(5), 2200646:1-10 (2023)
doi:10.1002/pssa.202200646

Publications without peer review

M. Grundmann: *Thin Film Electronics from Amorphous Oxide and Halogen Semiconductors*, BuildMoNa Annual Report 2021, p. 27-29 (2023)

R. Hildebrandt, M. Seifert, J. George, S. Blaurock, S. Botti, H. Krautscheid, M. Grundmann, C. Sturm: *Temperature dependent second-order Raman scattering in CuI*, arxiv: 2305.18931 (2023)
doi:10.48550/arXiv.2305.18931

J.K. Jochum, M. Lorenz, H.P. Gunnlaugsson, C. Patzig, T. Höche, M. Grundmann, A. Vantomme, K. Temst, M.J. Van Bael, V. Lazenka: *Impact of magnetization and hyperfine field distribution on high magnetoelectric coupling strength in* $BaTiO_3$*-*$BiFeO_3$ *multilayers*, arxiv: 2303.08493 (2023)
doi:10.48550/arXiv.2303.08493

Patents

M. Grundmann: *DEVICE FOR CONDUCTING RADIATION, A PHOTODETECTOR ARRANGEMENT, AND A METHOD FOR SPATIALLY RESOLVED SPECTRAL ANALYSIS*, US 11,543,346 B2 (United States Patent, 2023)

Talks

C. Dethloff, S. Vogt, D. Splith, H. vvon Wenckstern, M. Grundmann: *Physical properties of $Ni_xCu_{1-x}I$ thin films deposited by magnetron co-sputtering*, DPG Spring Meeting, Dresden, Germany, March 2023

C. Dethloff, S. Vogt, D. Splith, H. von Wenckstern, M. Grundmann: *Physical properties of $Ni_xCu_{1-x}I$ thin films deposited by magnetron co-sputtering*, Annual BuildMoNa Conference, Leipzig, Germany, April 2023

C. Dethloff, S. Vogt, D. Splith, S. Selle, K. Thieme, H. von Wenckstern, M. Grundmann: *Ni-Cu-I alloy - a novel dilute magnetic semiconductor*, EMRS Fall Meeting, Warsaw, Poland, September 2023

S. Henn, M. Grundmann, C. Sturm: *Imaging Ellipsometry For Photonic Guided Mode Detection*, 12th Workshop on Spectroscopic Ellipsometry, Prague, Czech Republic, 2023

A. Jörns, H. von Wenckstern, M. Grundmann: *Simulating multi-component target ablation: A new pulsed laser deposition technique*, EMRS Fall Meeting, Warsaw, Poland, September 2023

E. Krüger, M. Seifert, V. Gottschalch, H. Krautscheid, C.S. Schnohr, M. Grundmann, C. Sturm: *Optical properties of $Ag_xCu_{1-x}I$ alloy thin films*, DPG Spring Meeting, Dresden, Germany, March 2023

C. Petersen, H. von Wenckstern, M. Grundmann: *Analysis of thickness distributions for combinatorial pulsed laser deposition*, DPG Spring Meeting, Dresden, Germany, March 2023

C. Petersen, H. von Wenckstern, M. Grundmann: *Analysis of thickness distributions for combinatorial pulsed laser deposition*, Annual Build Mona Conference, Leipzig, Germany, March 2023

C. Petersen, S. Vogt, H. von Wenckstern, M. Grundmann: *Pulsed Laser Deposition of α-Ga_2O_3 on m-Plane Al_2O_3: Growth Regime, Growth Process and Structural Properties*, Compound Semiconductor Week, Jeju, South Korea, May 2023

T. Stralka, S. Vogt, C. Dethloff, J. Bredow, H. von Wenckstern, M. Grundmann: *Current probe AFM measurements on reactively co-sputtered $Ag_xCu_{1-x}I$ thin films*, DPG Spring Meeting, Dresden, Germany, March 2023

C. Sturm: *Ellipsometry on optically anisotropic materials*, 12th Workshop on Spectroscopic Ellipsometry, Prague, Czech Republic, 2023 (invited)

C. Sturm: *Electromagnetic Waves in Crystals: The Presence of Exceptional Points*, 3rd International Workshop Biophotonics and Optical Angular Momentum, Palaiseau, France, September 2023 (invited)

C. Sturm: *Singular axes in anisotropic materials*, Nebraska Ellipsometry Lecture Mini Series, October, 2023 (invited/online)

L. Thyen, D. Splith, M. Kneiß, H. von Wenckstern, M. Grundmann: *Characterization and optimization of (Mg,Zn)O thin films with steep lateral composition gradient*, DPG Spring Meeting, Dresden, Germany, March 2023

S. Vogt, C. Dethloff, J. Bredow, T. Stralka, H. von Weckstern, M. Grundmann: *On the influence of the cation composition on reactively co-sputtered $Ag_xCu_{1-x}I$ thin films: Characterization of electrical, optical and structural properties*, DPG Spring Meeting, Dresden, Germany, March 2023

S. Vogt, C. Petersen, T. Schultz, H. von Wenckstern, N. Koch, M. Grundmann: *Exploration of zirconium doping in pulsed laser deposited alpha-Ga_2O_3*, EMRS Fall Meeting, Warsaw, Poland, September 2023

H. von Wenckstern: *An Introduction to and current examples of combinatorial material science*, MATS - Solar Cell Materials Seminar, Oslo, Norway, March 2023 (invited)

H. von Wenckstern: *Creation of Material Libraries by Pulsed Laser Deposition – History and Recent Developments*, EMRS Spring Meeting, Strasbourg, France, June 2023 (invited)

J. Yu, S. Luo, M. Grundmann: *Heteroepitaxial Growth of Ultrawide Bandgap Cubic Spinel Zn_2GeO_4 Thin Films by Pulsed Laser Deposition*, DPG Spring Meeting, Dresden, Germany, March 2023

Posters

J. Bredow, S. Vogt, C. Dethloff, H. von Wenckstern, M. Grundmann: *Heterostructure diodes based on reactively co-sputtered $Ag_xCu_{1-x}I$ thin films*, DPG Spring Meeting, Dresden, Germany, March 2023

F. Dobener, M. Müller, C. Emminger, C. Sturm, T. Haraszti, M. Grundmann, S. Brockhauser: *Developing an open source ellipsometry analysis workflow*, DPG Spring Meeting, Dresden, Germany, March 2023

K. Dorywalski, N. Lemee, C. Sturm, M. Grundmann, *Effect of epitaxial growth on the optical properties of $PbTiO_3$ perovskite oxide thin and ultra-thin films*, 12th Workshop on Spectroscopic Ellipsometry, Prague, Czech Republic, 2023

P. Firme, C. Brunhuber, L. Trefflich, P. Schlupp, D. Splith, H. von Wenckstern, C. Sturm, M. Grundmann: *Graded $Zn_{1-x}Mg_xO$ layers as building blocks for ultra-compact wavemeters*, DPG Spring Meeting, Dresden, Germany, March 2023

S. Henn, M. Grundmann, C. Sturm: *Strongly Coupled Bloch Surface Wave Polaritons In ZnO Above Room Temperature*, Annual Build MoNa Conference, Leipzig, Germany, March 2023

S. Henn, M. Grundmann, C. Sturm: *Optical Grating Couplers For The Excitation Of Bloch Surface Waves*, DPG Spring Meeting, Dresden, Germany, March 2023

S. Henn, M. Grundmann, C. Sturm: *Imaging Ellipsometry For Photonic Guided Mode Detection*, 12th Workshop on Spectroscopic Ellipsometry, Prague, Czech Republic, 2023 (awarded)

A. Jörns, H. von Wenckstern, M. Grundmann: *Simulating multi-component target ablation: A new pulsed laser deposition technique*, DPG Spring Meeting, Dresden, Germany, March 2023

A. Jörns, H. von Wenckstern, M. Grundmann: *Simulating multi-component target ablation: A new pulsed laser deposition technique*, Compound Semiconductor Week, Jeju, South Korea, May 2023

A. Jörns, H. von Wenckstern, M. Grundmann: *Copper tin oxide: An amorphous ternary oxide system with tunable optical and electrical properties*, Compound Semiconductor Week, Jeju, South Korea, May 2023

A. Jörns, H. von Wenckstern, M. Grundmann: *Copper tin oxide: An amorphous ternary oxide system with tunable optical and electrical properties*, EMRS Fall Meeting, Warsaw, Poland, September 2023

E. Krüger, V. Gottschalch, G. Benndorf, R. Hildebrandt, A.L. Pereira, M. Bar, S. Blaurock, S. Merker, C. Sturm, M. Grundmann, H. Krautscheid: *Epitaxial growth of $Ag_xCu_{1-x}I$ on Al_2O_3 (0001)*, DPG Spring Meeting, Dresden, Germany, March 2023

E. Krüger, S. Merker, R. Hildebrandt, A.L. Pereira, L. Käferstein, S. Blaurock, H. Krautscheid, M. Grundmann, and C. Sturm: *Exciton-polariton emission in copper halides*, DPG Spring Meeting, Dresden, Germany, March 2023

K.E. McGhee, M. Guizzardi, R. Jayaprakash, K. Georgiou, G. Cerullo, A. Zasedatelev, T. Virgili, P.G. Lagoudakis, D.G. Lidzey: *Ultrafast optical control of polariton energy in an organic semiconductor microcavity*, DPG Spring Meeting, Dresden, Germany, March 2023

A. Müller, S. Henn, E. Krüger, S. Blaurock, H. Krautscheid, M. Grundmann, C. Sturm: *Multiphoton absorption induced photoluminscence in CuI*, DPG Spring Meeting, Dresden, Germany, March 2023

A.L. Pereira, R. Hildebrandt, J. Bredow, C. Dethloff, V. Gottschalch, S. Vogt, H. Krautscheid, M. Grundmann, C. Sturm: *Raman spectra of CuI alloys with Ag and Br*, DPG Spring Meeting, Dresden, Germany, March 2023

C. Petersen, S. Vogt, H. von Wenckstern, M. Grundmann: *Pulsed Laser Deposition of α-Ga_2O_3 on m-Plane Al_2O_3: Growth Regime, Growth Process and Structural Properties*, GOx 2023, Buffalo (New York), USA, August 2023

C. Petersen, S. Köpp, D. Splith, H. von Wenckstern, M. Grundmann: *α-Ga_2O_3 based Schottky Barrier Diodes: Influence of Schottky-Contact Metal and Deposition Method*, EMRS Fall Meeting, Warsaw, Poland, September 2023

C. Petersen, S. Köpp, H. von Wenckstern, M. Grundmann: *α-Ga_2O_3 based Schottky Barrier Diodes: Choice of Schottky Metal*, Compound Semiconductor Week, Jeju, South Korea, May 2023

L. Trefflich, M. Callmeier, C. Walter, M. Seifert, S. Botti, H. von Wenckstern, M. Grundmann, C. Sturm: *Dielectric function of β-CuI*, 12th Workshop on Spectroscopic Ellipsometry, Prague, Czech Republic, 2023

5

Graduations

Doctorate

- Oliver Lahr
  Toward Sustainable Transparent and Flexible Electronics with Amorphous Zinc Tin Oxide
  March 2023
- Richard Busch
  Three-Dimensional Microstructure Characterization of Surface-Crystallized Glass Ceramics
  October 2023
- Evgeny Krüger
  Optical Transitions and Charge Carrier Dynamics in Copper and Silver Halides
  November 2023

Master

- Sandra Montag
  Structural and Electric Characterisation of Cubic Indium Gallium Oxide
  January 2023
- Khanim Karimova
  PLD Deposition of Copper Iodide Thin Films and Heterostructures Utilising Sodium Halides
  January 2023
- Mauricio Bassallo
  Fabrication and Characterization of Schottky Photodetectors on Laterally Graded Mg[t]x[/t]Zn[t]1[/t][t]-[/t][t]x[/t]O Thin Film
  April 2023
- Arthur Rubin Witte
  Simulation of Coplanar Waveguides for Microwave Pulses
  April 2023
- Felix-Florian Delatowski
  Bestimmung der dielektrischen Funktion von CuI Dünnfilmen in CuI-Al_2O_3 Mehrschichtsystemen bei verschiedenen Wachstumsparametern
  May 2023

- Jorrit Bredow
  Reactively Co-Sputtered $Ag_xCu_{1-x}I$: Growth Study and First Heterostructures
  September 2023

Bachelor

- Doyeon Jin
  Pulsed Laser Deposition of Ni doped CuI Thin Films on C-plane Sapphire: Growth and Characterization
  March 2023
- Ana Lucia Pereira Brenes
  Characterization of the Phononic Properties of $CuBr_xI_{1-x}$ and $Cu_{1-x}Ag_xI$ via Raman Spectroscopy, April 2023
- Caspar Pirker
  Geometrisch-numerische Berechnung der Zusammensetzung von VCCS-PLD Dünnfilmen für beliebige Segmentierungsformen
  May 2023
- Visar Demiri
  Laser-Induced Plasma Etching (LIPE) of polyimide-foils
  September 2023
- Martin Callmeier
  Estimation of the Dielectric Function of β-CuI
  October 2023

6

Guests

- Jingjing Yu
  Ningbo Institute of Materials Technology & Engineering (NIMTE), Ningbo, PR China
  China Scholarship Council
  August 2020 – August 2024

Author Index

B

Blaurock, S. 36
Brunhuber, C. 41

F

Frodason, Y.K. 32

G

GarciaFernandez, J. 33
Gierth, S. 19
Grundmann, M. . 17, 19, 25, 27, 29, 30, 32, 33, 35, 36, 38, 41, 43

H

Hammud, A. 30
Henn, S. 38
Hildebrandt, R. 35

J

Jörns, A. 27

K

Karsthof, R. 32
Kneiss, M. 30, 33
Koch, N. 25, 30
Krautscheid, H. 36
Käferstein, L. 36

L

Langorgen, A. 32
Lorenz, M. 19
Luo, S. 21

M

Montag, S. 33
Müller, A. 36, 38

P

Petersen, C. 25
Prytz, O. 33

S

Schlupp, P. 27
Schultz, T. 25, 30
Schöppach, F. 29
Selle, S. 19
Splith, D. 29, 30, 33, 41
Storm, P. 19, 30
Sturm, C. 35, 36, 41, 43

T

ThueJensen, I.J. 32
Trefflich, L. 21, 36, 41

V

Vines, L. 32
Vogt, S. 25, 27
von Wenckstern, H. . . 19, 27, 29, 30, 32, 33

2023 SEMICONDUCTOR PHYSICS UNIVERSITÄT LEIPZIG

Vol. 5 • No. 4 • April 2024

ADVANCED PHOTONICS RESEARCH

Open Access

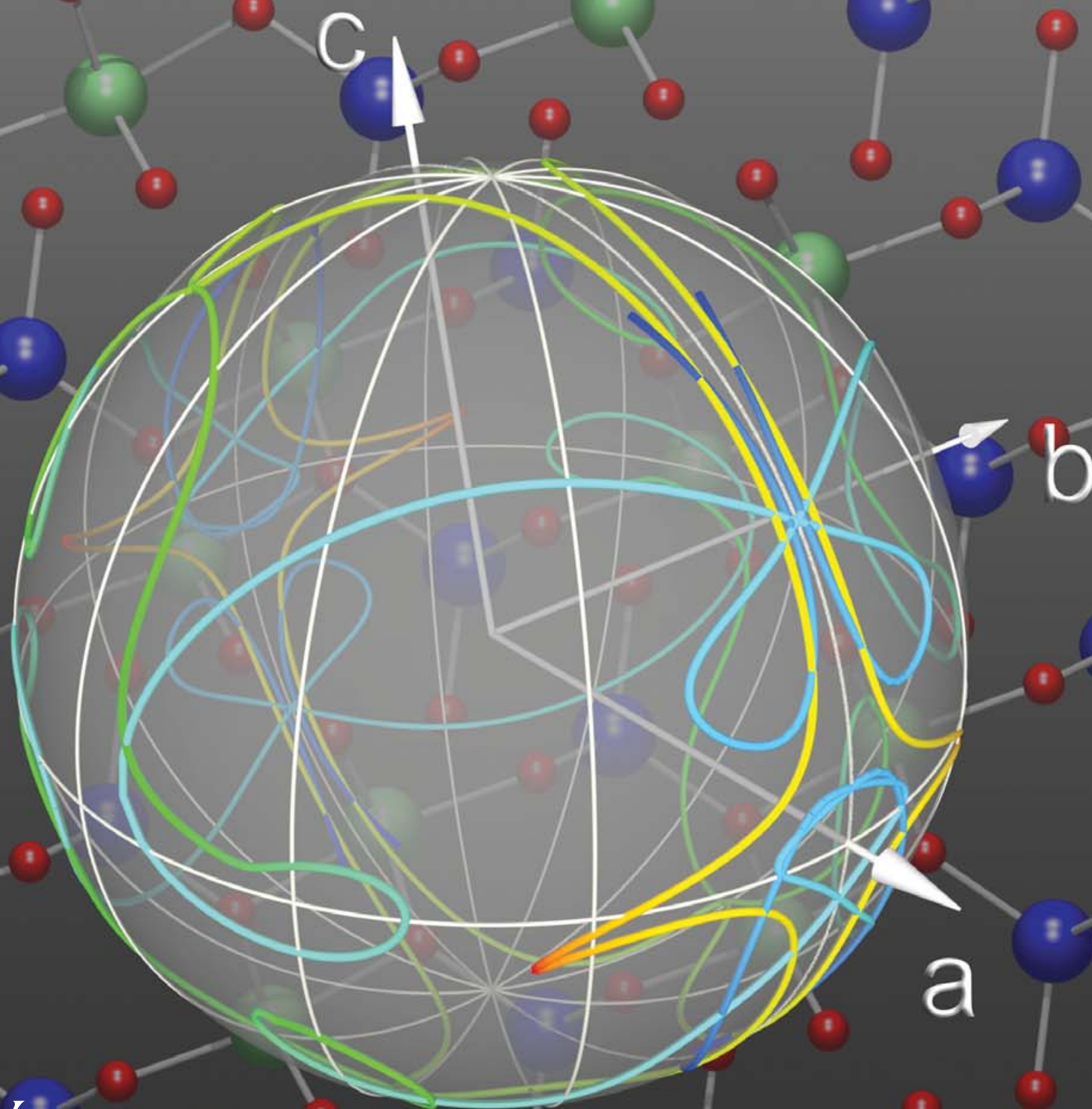

WILEY-VCH

www.advphotonicsres.com